A Technical Memorandum 4230

ernal Performance of a Hybrid

symmetric/Nonaxisymmetric

vergent-Divergent Nozzle

E. Taylor

RY 1991

NASA Technical Memorandum 4230

Internal Performance of a Hybrid Axisymmetric/Nonaxisymmetric Convergent-Divergent Nozzle

John G. Taylor
Langley Research Center
Hampton, Virginia

Summary

An investigation has been conducted in the static test facility of the Langley 16-Foot Transonic Tunnel to determine the internal performance of a hybrid axisymmetric/nonaxisymmetric nozzle in forward-thrust mode. Nozzle cross sections in the spherical convergent section were axisymmetric, whereas cross sections in the divergent flap area were non-axisymmetric (two dimensional). Nozzle concepts simulating dry and afterburning power settings were investigated. Both subsonic cruise and supersonic cruise expansion ratios were tested for the dry power nozzle concepts. Afterburning power configurations were tested at an expansion ratio typical of subsonic acceleration. The spherical convergent flaps were designed in such a way that the transition from axisymmetric to nonaxisymmetric cross section occurred in the region of the nozzle throat. Three different nozzle throat geometries were tested for each nozzle power setting. High-pressure air was used to simulate the jet exhaust at nozzle pressure ratios up to 12.

Static internal thrust ratio, discharge coefficient, and static pressure data indicate that the most efficient design (the highest level of internal thrust ratio) requires convergence of the nozzle internal cross-sectional area up to the divergent flap hinge, thus allowing for the internal flow to pass through the transition from axisymmetric to nonaxisymmetric in a region of subsonic flow. This provides higher thrust levels and discharge coefficients with more two-dimensional lateral pressure distributions on the nozzle divergent flaps.

Introduction

Many studies have shown that the performance of fighter aircraft would benefit from the incorporation of thrust-vectoring technology into their exhaust nozzles (refs. 1 to 13). Thrust vectoring can allow aircraft to operate at lower speeds than conventional aircraft (allowing short takeoff and landing capability, see refs. 5 to 8) and at very high angles of attack that occur during "super-maneuverability" or post-stall maneuvering (refs. 9 to 13). One nozzle design that lends itself to modifications for providing multiaxis thrust vectoring is the two-dimensional convergent-divergent (2-D C-D) nozzle.

Several investigations into 2-D C-D multiaxis thrust-vectoring nozzles have shown that by simultaneous deflection of the divergent flaps, pitch thrust vectoring can be accomplished with small or no losses in resultant thrust ratio, and resultant vector angles equal to the geometric angle can be achieved (refs. 14 to 18). This can be attributed to the fact that the di-

vergent flaps provide large flow-turning surfaces, and when deflected they typically force a physical shift in the throat location that results in subsonic flow turning. Unfortunately, yaw thrust-vectoring capability is not as easily integrated into a standard 2-D C-D nozzle geometry as pitch thrust-vectoring capability. Results from the static test facility of the Langley 16-Foot Transonic Tunnel have shown that yaw thrust vectoring typically results in decreased nozzle efficiency and resultant yaw vector angles lower than the geometric angle (refs. 19 to 22). In addition, nozzles with multiaxis thrust-vectoring capabilities tend to be much heavier than similar nozzles without these capabilities.

A hybrid axisymmetric/nonaxisymmetric nozzle, herein called the spherical convergent flap (SCF) nozzle, has been designed to provide efficient simultaneous pitch and yaw thrust-vectoring capability and reduced nozzle weight in comparison with other 2-D C-D multiaxis thrust-vectoring nozzles. (See ref. 14.) The SCF nozzle accomplishes these tasks with an axisymmetric convergent section coupled to a nonaxisymmetric two-dimensional divergent section. It provides yaw thrust vectoring by way of a gimballing mechanism integrated into the nozzle convergent flaps. Pitch thrust vectoring is achieved by simultaneous deflection of the upper and lower two-dimensional divergent flaps. The nozzle weight is reduced because the gimballing mechanism is integrated efficiently into the structure of the axisymmetric convergent section and the typical transition section is deleted. The spherical convergent flaps were designed in such a way that the transition from axisymmetric to nonaxisymmetric cross section occurred in the region of the nozzle throat.

In the design of the SCF nozzle, it was realized that there were several options available for the transition geometry in the throat region. It was essential to determine the internal geometry required for optimum performance in the forward-thrust mode before investigating the thrust-vectoring capabilities of this nozzle design because a nozzle typically operates in the forward-thrust mode during most of the flight envelope. Investigations into the thrust-vectoring capabilities of the SCF nozzle have been conducted and results are reported in reference 14.

The present investigation was conducted in the static test facility of the Langley 16-Foot Transonic Tunnel to determine the internal performance of a hybrid axisymmetric/nonaxisymmetric nozzle in forward-thrust mode. Nozzle cross sections in the spherical convergent section were axisymmetric, whereas cross sections in the divergent flap area were nonaxisymmetric (two dimensional). Nozzle concepts simulating dry and afterburning power settings

1

were investigated. Both subsonic cruise and supersonic cruise expansion ratios were tested for the dry power nozzle concepts. Afterburning (A/B) power configurations were tested at an expansion ratio typical of subsonic acceleration. Three different nozzle throat geometries were tested for each nozzle power setting, resulting in nine different test configurations. High-pressure air was used to simulate jet exhaust at nozzle pressure ratios up to 12.

Symbols

A detailed discussion of the data reduction and calibration procedures can be found in references 23 and 24. Definitions of propulsion relationships used in this report can be found in reference 24.

A_e — nominal nozzle exit area, in^2

A_t — measured nozzle throat area, in^2

C_d — nozzle discharge coefficient, w_p/w_i

F — measured thrust along body axis, lbf

F/F_i — internal thrust ratio

F_i — ideal isentropic gross thrust, lbf,

$$w_p\sqrt{\frac{2\gamma R_j}{(\gamma-1)g}}\sqrt{(T_{t,j}+459.67)\left[1-\left(\frac{1}{NPR}\right)^{\frac{\gamma-1}{\gamma}}\right]}$$

g — acceleration due to gravity ($1g \approx 32.174$ ft/sec^2)

h_t — nominal nozzle throat height, in.

L — axial length of divergent flaps, 2.87 in.

NPR — nozzle pressure ratio, $p_{t,j}/p_a$

$(NPR)_d$ — design nozzle pressure ratio (NPR for fully expanded flow at nozzle exit)

p — local static pressure, psi

p_a — atmospheric pressure, psi

$p_{t,j}$ — jet total pressure, psi

$p/p_{t,j}$ — static pressure ratio

R_j — gas constant, 53.3643 ft/°R

$T_{t,j}$ — jet total temperature, °F

w_i — ideal weight-flow rate, lbf/sec,

$$A_t p_{t,j}\,\frac{2}{\gamma+1}^{\frac{\gamma+1}{2(\gamma-1)}}\sqrt{\frac{\gamma g}{R_j(T_{t,j}+459.67)}}$$

w_p — measured weight-flow rate, lbf/sec

w_t — nominal nozzle throat width, 3.05 in.

x — axial distance from divergent flap hinge to static pressure orifice

y — horizontal distance from model centerline to static pressure orifice

z — vertical distance from model centerline to static pressure orifice

α — divergence angle of upper and lower divergent flaps, deg

γ — ratio of specific heats, 1.3997 for air

ϕ — orifice radial angle, positive in clockwise rotation looking upstream (see fig. 5), deg

Abbreviations:

A/B — afterburning

SCF — spherical convergent flap

Sta — model station, in.

2-D C-D — two-dimensional convergent-divergent

Apparatus and Methods

Description of Static Test Facility

Model testing was conducted in the static test facility of the Langley 16-Foot Transonic Tunnel. The model was located in a large room where the jet exhaust from a simulated single-engine propulsion system was vented to the atmosphere. This facility utilized the same clean, dry, high-pressure air supply as that used in the 16-Foot Transonic Tunnel and a similar air control system, which included valving, filters, and a heat exchanger (used to maintain a constant temperature in the high-pressure plenum). A remotely located control room contained the controls for the airflow valves and a closed-circuit television to observe the model when the jet was operating.

Simulated Single-Engine Propulsion System

A sketch of the single-engine, air-powered nacelle model on which the various nozzle models were tested is presented in figure 1(a). A photograph of the simulated propulsion system is shown in figure 1(b) with a typical spherical convergent flap (SCF) configuration installed.

An external high-pressure air system provided a continuous flow of clean, dry air at a controlled temperature of approximately 85°F. This high-pressure air was varied during jet simulation up to about

12 atm. The model was secured on a support strut through which the pressurized air was routed. The air traveled through tubing in the strut into a high-pressure plenum chamber. From there the air was discharged perpendicularly into the low-pressure plenum through eight multiholed, equally spaced sonic nozzles located around the high-pressure plenum. (See fig. 1(c).) This airflow system was designed to minimize any forces incurred during the transfer of axial momentum as the air is passed from the nonmetric (not on the balance) high-pressure plenum to the metric (on the balance) low-pressure plenum.

A pair of flexible metal bellows (shown in fig. 1(c)) sealed the air system between the metric and nonmetric parts of the model and compensated for any axial force caused by pressurization. The low-pressure air then passed from the circular low-pressure plenum through a circular multiple-orifice choke plate (flow straightener) and a circular instrumentation section, which was common for all nozzle models tested. All nozzle configurations were attached to the instrumentation section at model station (Sta) 39.00.

Nozzle Design

An area reduction section (shown in fig. 2) was attached downstream of the round instrumentation section to decrease the cross-sectional area of the duct so that the ratio of duct area to nozzle geometric throat area would closely resemble current engine afterburner duct/nozzle sizing. It was necessary to decrease the duct area in order to increase the duct Mach number to an appropriate level of approximately 0.27, typical of afterburning ducts in current turbojet engines.

All spherical convergent flap sections were attached to the downstream end of the reduction section at station 41.65. The spherical convergent flap sections formed the transition region from axisymmetric to nonaxisymmetric cross section. The internal flow traveled through the axisymmetric compression region and turned over a lip onto a planar surface just upstream of the hinge for the divergent flaps. (See figs. 3 and 4.) The planar surfaces of the upper and lower convergent flaps formed an angle with respect to the model centerline. Three different convergent flap throat angles were tested in this investigation for both dry power and afterburning (A/B) power configurations. Similar internal shaping in the convergent flap region formed the sides of the SCF nozzle, which were parallel to the model centerline.

For the dry power settings, the three convergent flap throat geometries tested were called the 18°, 0°, and −18° configurations. The designations of 18°, 0°,

and −18° came from nominal angles in the design of these configurations. The actual angles of the planar surfaces between the convergent flap lip and divergent flap hinge varied from these nominal values because of fabrication processes. The planar surfaces of the 18° configuration (upper and lower) diverged 19°1′ from the model centerline on the downstream side of the spherical convergent flap lip and extended to the divergent flap hinge.

The minimum internal area for this configuration had a three-dimensional iris shape that was upstream of the divergent flap hinge between the hinge and the convergent flap lip. It was not possible to accurately measure this area. The planar surfaces of the 0° configuration were designed and measured to be parallel to the model centerline between the convergent flap lip and the divergent flap hinge. This created a constant area duct of two-dimensional cross section, providing a passage of minimum internal area for the nozzle throat. The planar surfaces of the −18° configuration converged (at a 15° angle to the model centerline) from the convergent flap lip to the divergent flap hinge. This forced the minimum area to occur at the divergent flap hinge ($x = 0$). Because of difficulties measuring the minimum area on the 18° configuration, the throat area for all dry power configurations was measured at the divergent flap hinge. This also gives a common reference point for later comparison of discharge coefficient data. Note that the subsonic cruise and supersonic cruise configurations employed the same spherical convergent flap sections but utilized different sets of divergent flaps.

For the A/B power settings, the three convergent flap throat geometries tested were called the 35°, 17°, and 0° configurations. The planar surfaces of the 35° configuration diverged 35°35′ from the model centerline on the downstream side of the spherical convergent flap lip, extending to the divergent flap hinge. The planar surfaces of the 17° configuration diverged 18° from the model centerline on the downstream side of the spherical convergent flap lip, extending to the divergent flap hinge. For both of these configurations, the minimum geometric internal area had a three-dimensional iris shape that was near the convergent flap lip and extended over to the sidewalls. Again, it was not possible to accurately measure this area. The planar surfaces of the 0° configuration were parallel to the model centerline between the convergent flap lip and the divergent flap hinge. Again, this created a constant area duct of minimum internal area for the nozzle throat. Because of difficulties measuring the minimum area on the 35° and 17° configurations, the throat area for the A/B power configurations was also measured at the divergent

3

flap hinge. The designations of 35°, 17°, and 0° came from nominal angles in the design of these configurations. The actual angles of the planar surfaces again varied from these nominal values because of model fabrication processes.

The throat angle of the spherical convergent flap for a dry power configuration changed when the convergent flaps were opened up to go to maximum A/B operation. The relationship between the throat angles of the dry and A/B power configurations for the SCF nozzle is explained below for the three geometries examined. The planar sections of the spherical convergent flaps formed a nominal angle of 18° with the nozzle centerline when the nozzle was operating at dry power conditions. When the convergent flaps were moved to open up the throat area of the nozzle (to go from dry to A/B power), the planar surfaces moved to an angle of 35°. Correspondingly, when the planar sections of the convergent flaps formed an angle of 0° with the nozzle centerline at dry power, the flaps moved to an angle of 17° when in A/B power. When the planar section of the convergent flaps formed a nominal angle of $-18°$ with the nozzle centerline in dry power, the flaps correspondingly moved to an angle of 0° when in A/B power.

As stated earlier, nozzle throat areas were measured at the divergent flap hinge because of the difficulty of measurement of certain configurations and in order to have a common reference point. These measured areas are tabulated in figure 4. The dry power nozzle configurations were tested at an expansion ratio of 1.35 ($\alpha = 4.58°$, $(\text{NPR})_d = 5.03$) for a subsonic cruise nozzle and at an expansion ratio of 2.00 ($\alpha = 12.86°$, $(\text{NPR})_d = 10.65$) for a supersonic cruise nozzle. The maximum A/B configurations were tested at an expansion ratio of 1.20 ($\alpha = 4.58°$, $(\text{NPR})_d = 3.86$). Of all the configurations tested, only the $-18°$ dry power configurations had decreasing cross-sectional internal area all the way to the divergent flap hinge plane.

Instrumentation

A thermocouple and a pressure probe located in the high-pressure plenum supplied temperature and pressure measurements used to calculate the weight-flow rate of the high-pressure air supplied to the model. A thermocouple was positioned in the instrumentation section to measure the jet total temperature. A rake with five total pressure probes and an additional total pressure probe were located in the instrumentation section to measure the jet total pressure. (See fig. 1(a).) An average of the six jet total pressure measurements was used for the jet total pressure $p_{t,j}$. Measured values of the temperature and pressure in the instrumentation section, along with the measured nozzle throat area, were used to compute the ideal weight-flow rate. Details of the measured and ideal weight-flow rate calculations can be found in reference 24. A six-component strain gauge balance was used to measure the forces and moments on the model downstream of station 20.50. The balance moment reference center was located on the centerline at station 29.39.

A maximum of 49 static pressures were measured on the dry power configurations, and 48 static pressures were measured on the A/B power configurations. A total of 36 static pressure orifices were located downstream of the divergent flap hinge. Twenty-four orifices were located on the upper divergent flap and 12 were located on the right sidewall. Static pressure orifices were located on the top centerline and side centerline of the nozzle convergent flaps with two more orifices located just upstream of the convergent flap lip (between the centerline and the sidewall, shown in fig. 5). Static pressure orifice locations were measured from the divergent flap hinge plane (also considered to be the nozzle geometric throat plane, $x = 0$) and were nondimensionalized with respect to the divergent flap length L, divergent flap half-width $w_t/2$, or nozzle throat half-height $h_t/2$. These static pressure orifice locations $\left(x/L, \frac{y}{w_t/2}, \text{ and } \frac{z}{h_t/2}\right)$ are presented in tables 1 to 3 and figure 5. Static pressure ($p/p_{t,j}$) data are given in tables 4 to 12 for all configurations investigated.

Data Reduction

All data were recorded on magnetic tape and taken in ascending order of $p_{t,j}$. Fifty frames of data, taken at a rate of 10 frames per second, were used to compute an average value for each data point. The basic performance parameters used in the presentation of results were internal thrust ratio F/F_i, nozzle discharge coefficient C_d, and the ratio of internal static pressure to the average jet total pressure $p/p_{t,j}$.

The internal thrust ratio F/F_i is the ratio of measured nozzle thrust along the body axis to ideal thrust where ideal thrust is based upon measured weight-flow rate w_p, jet total temperature $T_{t,j}$, and nozzle pressure ratio NPR. The balance axial-force measurement, from which the actual nozzle thrust F is subsequently obtained, is initially corrected for balance interactions. Although the bellows arrangement was designed to eliminate pressure and momentum interactions with the balance, small bellows tares on the six balance components still exist. These tares result from a small pressure difference between the ends of the bellows when internal velocities are high and from small differences in the spring constants of the forward and aft bellows when the bellows are

pressurized. These bellows tares were determined by testing standard axisymmetric calibration nozzles with known performance over a range of expected nozzle pressure ratios. The balance data were then corrected in a manner similar to that discussed in reference 24 to obtain thrust along the body axis F.

Losses included in the thrust term F, which cause values of F/F_i to fall below 1.0, are caused by friction and pressure drags associated with the nozzle hardware. In addition, overexpansion and underexpansion losses occur when the nozzle is not operating at the design nozzle pressure ratio. These losses are caused by momentum losses incurred when the velocity vectors at the nozzle exit plane are not aligned with the thrust axis.

The nozzle discharge coefficient C_d is the ratio of measured weight-flow rate to ideal weight-flow rate, where ideal weight-flow rate is dependent upon jet total pressure $p_{t,j}$, jet total temperature $T_{t,j}$, and measured nozzle throat area A_t. The measured weight-flow rate w_p was determined from the procedure given in reference 24. The nozzle discharge coefficient reflects the efficiency with which a nozzle passes weight flow and is reduced by any momentum and vena contracta losses (ref. 25). Obviously, an inaccurate measurement of the throat area (due to three-dimensionality, for example) would bias values of nozzle discharge coefficient. This bias cannot be separated from actual changes in nozzle discharge coefficient related to the aforementioned phenomenon.

Test Procedure

All configurations were tested over a range of nozzle pressure ratios (for dry power, 1.8 up to 12.1; for A/B power, 1.8 up to 7.8), with NPR being increased until a balance limit was reached. For all configurations, data were taken in ascending order of $p_{t,j}$, and the temperature in the high-pressure plenum was held constant throughout the test at 85°F to prevent condensation in the divergent section of the nozzle as the flow was expanded to ambient conditions.

Results

There were nine spherical convergent flap configurations tested in this investigation (three dry power subsonic cruise, three dry power supersonic cruise, and three maximum A/B subsonic acceleration). Internal thrust ratio, discharge coefficient, and internal static pressure distributions are presented in figures 6 to 11. Dry power data for both subsonic (figs. 6 and 7) and supersonic (figs. 8 and 9) cruise expansion ratios indicated that the $-18°$ configurations performed the most efficiently (had the highest

peak internal thrust ratio) of the three throat designs. Correspondingly, the afterburning power data (figs. 10 and 11) indicated that the 0° configuration attained the highest performance of the three A/B power throat geometries tested. Similar trends were seen in the discharge coefficient data. (The highest levels of discharge coefficient were measured on the $-18°$ dry power concept and the 0° A/B power concept. For the other configurations tested, however, it cannot be determined whether the increased losses in C_d were due to the actual nozzle efficiency or to the incorrect measurement of the actual nozzle throat area.) Recall from the discussion of nozzle geometry that these are corresponding configurations. (When the convergent flaps are opened up, the $-18°$ dry throat transitions to the 0° A/B throat.)

For the dry power subsonic cruise configurations, the $-18°$ concept achieved a peak internal thrust ratio of 0.988 at a nozzle pressure ratio of 6. (See fig. 6(a).) This nozzle pressure ratio corresponds to an effective expansion ratio of 1.47, which is higher than the geometric expansion ratio $(A_e/A_t = 1.35,$ $(NPR)_d = 5.03)$. This difference between design and effective expansion ratio suggests that the effective nozzle throat area was smaller than the measured throat area. Values for discharge coefficient (presented in fig. 6(b)) remained nearly constant at a level near 0.965 over the nozzle pressure ratio range tested, about 2 percent lower than comparable 2-D C-D nozzles (refs. 15 and 18 to 20). The 0° throat concept attained its peak performance between a nozzle pressure ratio of 6 and 7. Therefore, the effective expansion ratio of this configuration was between the values of 1.47 and 1.59, again higher than the geometric expansion ratio. The discharge coefficient for this configuration was at a value of approximately 0.936, almost 3 percent lower than that for the $-18°$ configuration.

The peak internal thrust ratio for the 18° configuration occurred near a value of 0.972 at a nozzle pressure ratio of 8. This is a loss of 1.6 percent in peak thrust ratio when compared with the $-18°$ configuration. Again, the effective expansion ratio (corresponding to the NPR at peak F/F_i) of 1.71 is higher than the geometric value. A nearly constant value of 0.836 was measured for the discharge coefficient of this configuration, almost 13 percent lower than for the $-18°$ throat angle.

An examination of static pressure data (presented in fig. 7) indicated several possible reasons for the lower internal performance levels and lower values of discharge coefficient on the 0° and 18° subsonic cruise throat concepts when compared with the $-18°$ concept. All three concepts exhibited supersonic flow at and downstream of the divergent flap hinge.

5

Internal static pressure distributions along the convergent and divergent flap centerlines and at several spanwise locations on the divergent flap indicated that the $-18°$ subsonic cruise configuration generally had higher levels of static pressure (figs. 7(a) and 7(b)) and more two-dimensional flow patterns downstream of the nozzle throat (fig. 7(c)). Lateral pressure distributions on the divergent flaps (fig. 7(c)) had little variation as compared with the 0° and 18° configurations, indicating a well-behaved, nearly two-dimensional flow. The 0° and 18° configurations had much higher values of static pressure ratio (lower flow velocities) near the sidewalls just downstream of the divergent flap hinge, suggesting highly non-uniform flow exiting the lip region. It is likely that the shapes of the nozzle throats (the location at which $p/p_{t,j} = 0.528$) of the 0° and 18° configurations were more three dimensional than that of the $-18°$ nozzle concept, and it follows that flow non-uniformities and thrust losses would be higher.

A shift upstream in nozzle throat location to an effective area that is smaller than the measured nozzle throat area (which was measured at station 43.74 for dry power configurations for the divergent flap hinge) would lead to lower levels of discharge coefficient as well as higher effective expansion ratios. Both of these results were seen in the nozzle internal performance data presented in figure 6. Decreased C_d suggests an effectively lower nozzle throat area than the measured value of A_t used in data reduction. Recall from an earlier discussion that the minimum internal area on the 18° configuration had a three-dimensional shape that could not be measured accurately. If the minimum geometric nozzle internal area could have been measured, C_d would probably be higher than the values presented herein.

The fairing of the static pressure distributions along the sidewall centerline through the sonic throat region on either side of the divergent flap hinge (fig. 7(d)) was not well-defined by data. However, it appeared that the sonic condition occurred farther upstream for the 18° configuration than for the 0° and $-18°$ configurations. Nozzle geometry considerations, in combination with discharge coefficient data and sidewall static pressure distributions, indicate that the nozzle throat of the 18° configuration formed farther upstream than the sonic location for the 0° and $-18°$ configurations.

Although not shown, the two values of static pressure ratio measured just upstream of the convergent flap lip, off the centerline (see tables 4 to 6), indicated that at that location the Mach number was less than 0.6 ($p/p_{t,j} \geq 0.781$) for all three subsonic cruise configurations. Static pressure values just upstream of the divergent flap hinge on the centerline

indicated that the flow is supersonic for all configurations. Therefore, the sonic plane formed somewhere between the convergent flap lip and the divergent flap hinge. If in fact the physical throat on the 0° and 18° configurations is located farther upstream than that of the $-18°$ configuration, then supersonic flow is passing through a larger portion of the transition section from axisymmetric to nonaxisymmetric. This might have been another reason for the higher thrust losses. The $-18°$ configuration decreased in cross-sectional area all the way to the divergent flap hinge. As would be expected, this helped to force the sonic plane to form close to this hinge, allowing for the internal flow to pass through the transition from an axisymmetric cross section to a nonaxisymmetric cross section at subsonic speeds. Therefore, the $-18°$ configuration had a more uniform flow pattern (and therefore less thrust loss) than the patterns for the 0° and 18° configurations.

Similar data trends were seen for the dry power supersonic cruise concepts. (See figs. 8 and 9.) This might be expected when considering that the subsonic cruise and supersonic cruise configurations with the same throat angle employed identical spherical convergent flap sections. Effective expansion ratios for these three configurations were also higher than the geometric expansion ratio of 2.00. This was obvious because none of the internal thrust ratio curves had reached their peak at the corresponding design nozzle pressure ratio of 10.65. As the internal performance curves approached their peaks, the values of F/F_i for the $-18°$ concept were greater than those for the 0° and 18° configurations. The discharge coefficient was at approximately the same level for the supersonic cruise concept as for the corresponding subsonic cruise concept with the $-18°$ configuration having a higher C_d than both the 0° and 18° configurations. Static pressure distributions followed the same trends as the subsonic cruise concepts.

Recall from a previous discussion that as the convergent flaps are opened up to increase the nozzle throat area in going from dry to afterburning power, the $-18°$ dry power configuration would correspond to the 0° A/B power nozzle. Data trends for internal thrust ratio and discharge coefficient for A/B power configurations due to varying nozzle throat geometry (fig. 10) were similar to those for the dry power data. The 0° configuration performed the most efficiently of the three concepts tested. The nozzle peak internal thrust ratio for the 0° A/B power configuration ($F/F_i = 0.988$, shown in fig. 10(a)) occurs near a nozzle pressure ratio of 4 $(\text{NPR})_d = 3.86$, $A_e/A_t = 1.20$). The discharge coefficient leveled out at $F/F_i \approx 0.950$ over most of the nozzle pressure ratio range tested. The 17° throat configuration reached a peak value

of F/F_i of 0.979 at a nozzle pressure ratio near 5. The effective expansion ratio for this NPR is 1.35, higher than the geometric expansion ratio. A value of F/F_i of 0.904 was measured for the discharge coefficient for this concept. The lowest value of peak performance was measured on the 35° throat configuration at $F/F_i = 0.973$ for a nozzle pressure ratio of 6. This suggests an effective expansion ratio of 1.47, again higher than the geometric value of 1.20. Also, the lowest values of discharge coefficient (approximately 0.847) were measured on this configuration for the A/B power throat areas.

Again, it is likely that the physical throat area is less than that measured for the 35° and 17° configurations. This would give some reason for the large losses in discharge coefficient. However, the measured throat area has no effect on internal thrust ratio. Losses in peak internal thrust ratio are due to flow nonuniformity and the resultant increased viscous effects in the transition region.

Static pressure distributions for the maximum A/B power configurations are presented in figure 11. The 0° concept generally had higher levels of static pressure downstream of the divergent flap hinge (figs. 11(a) and 11(b)) and lower levels of flow nonuniformity (fig. 11(c)) than those for the 17° and 35° configurations. However, for the 0° configuration, lateral static pressure distributions on the divergent flaps (diamond symbols) did exhibit nonuniform flow patterns. Flow velocities near the sidewall were at a lower level than those near the nozzle centerline. Lateral static pressure distributions for the 0° A/B power configuration were similar to those for the 0° dry power configurations presented in figures 7(c) and 9(c). (See the square symbols.) These flow nonuniformities disappeared about halfway down the divergent flap.

Sidewall centerline static pressure distributions presented in figure 11(d) for the A/B power configurations were markedly different from those for the subsonic cruise configurations (fig. 7(d)). The sonic condition occurred farther upstream for the A/B power configurations (near $x/L = -0.12$), and there was little difference in the distributions upstream of the divergent flap hinge for the three geometries tested. All three configurations exhibit a slight flow compression at x/L between -0.1 and 0.1, and the 0° configuration had a subsonic bubble ($p/p_{t,j} = 0.531$) observed at $x/L = 0.104$. This bubble is probably a small recirculation region of separated flow just downstream of the sonic throat. Note that on this configuration, flow near the sidewall on the divergent flap surface at $x/L = 0.104$ was supersonic ($p/p_{t,j} = 0.396$ in fig. 11(c)).

The flow complexities caused by these A/B power throat geometries (none of which converged all the way to the divergent flap hinge) resulted in some flow nonuniformity downstream of the divergent flap hinge on all three configurations. However, discharge coefficient levels for the 0° A/B power configuration were higher than those for the 17° and 35° configurations. Similarly, the 0° A/B power configuration had a higher peak internal thrust ratio than the other two A/B power configurations tested. Note that although the peak internal thrust ratio of the 0° A/B power configuration was at the same level as that of the corresponding $-18°$ dry power subsonic cruise configuration, the discharge coefficient was about 1.5 percent lower. These results indicate that for maximum performance and minimum flow distortion, the convergent flap geometry must provide for convergence of the flow all the way to the divergent flap hinge plane.

Concluding Remarks

An investigation has been conducted in the static test facility of the Langley 16-Foot Transonic Tunnel to determine the internal performance of a hybrid axisymmetric/nonaxisymmetric nozzle in forward-thrust mode. Nozzle cross sections in the spherical convergent section were axisymmetric, whereas cross sections in the divergent flap area were nonaxisymmetric (two dimensional). Nozzle concepts simulating dry and afterburning power settings were investigated. Both subsonic cruise and supersonic cruise expansion ratios were tested for the dry power nozzle concepts. Afterburning (A/B) power configurations were tested at an expansion ratio typical of subsonic acceleration. Three different nozzle throat geometries were tested for each nozzle power setting. High-pressure air was used to simulate the jet exhaust at nozzle pressure ratios up to 12.

Results of this investigation indicate that the highest performance levels are obtained when the nozzle internal cross-sectional area decreases through the convergent flap section of the nozzle up to the divergent flap hinge plane. This type of design allows for more two-dimensional uniform flow patterns on the divergent flaps and a higher static pressure recovery. Although the 0° A/B configuration does not have convergence of the cross-sectional area to a minimum at the divergent flap hinge, it still had better performance and higher discharge coefficients than those configurations that geometrically diverged upstream of the divergent flap hinge.

NASA Langley Research Center
Hampton, VA 23665-5225
October 25, 1990

References

1. Ogburn, Marilyn E.; Nguyen, Luat T.; Wunschel, Alfred J.; Brown, Philip W.; and Carzoo, Susan W.: *Simulation Study of Flight Dynamics of a Fighter Configuration With Thrust-Vectoring Controls at Low Speeds and High Angles of Attack.* NASA TP-2750, 1988.

2. Murri, Daniel G.; and Nguyen, Luat T.: *Wind Tunnel Free-Flight Investigation of Thrust Vectoring Controls on a Forward-Swept-Wing Fighter Model.* NASA TP-2592, 1986.

3. Grafton, Sue B.: *Low-Speed Wind-Tunnel Free-Flight Investigation of Multiaxis Thrust-Vectoring Controls Applied to a Supersonic-Cruise Optimized Fighter Configuration.* NASA TP-2662, 1987.

4. Grafton, Sue B.; Croom, Mark A.; and Nguyen, Luat T.: *Low-Speed Wind-Tunnel Free-Flight Investigation of a Tailless Supersonic-Cruise Configuration Having an Integrated Thrust-Vectoring Control System.* NASA TP-2831, 1988.

5. Lander, J. A.; and Palcza, J. Lawrence: Exhaust Nozzle Deflector Systems for V/STOL Fighter Aircraft. AIAA Paper No. 74-1169, Oct. 1974.

6. Richey, G. K.; Surber, L. E.; and Berrier, B. L.: Airframe-Propulsion Integration for Fighter Aircraft. AIAA-83-0084, Jan. 1983.

7. Nelson, B. D.; and Nicolai, L. M.: Application of Multifunction Nozzles to Advanced Fighters. AIAA-81-2618, Dec. 1981.

8. *F-15 2-D Nozzle System Integration Study. Volume I—Technical Report.* NASA CR-145295, 1978.

9. Herbst, W. B.: Future Fighter Technologies. *J. Aircr.,* vol. 17, no. 8, Aug. 1980, pp. 561–566.

10. Herbst, W. B.: Supermaneuverability. *Workshop on Unsteady Separated Flow,* Michael S. Francis and Marvin W. Luttges, eds., AFOSR-TR-84-0911, U.S. Air Force, May 1984, pp. 1–9. (Available from DTIC as AD P004 153.)

11. Miller, L. Earl: *Post Stall Maneuvers and Thrust Vectoring Performance Analysis.* AFWAL-TR-84-3109, U.S. Air Force, July 1984. (Available from DTIC as AD A158 100.)

12. Herrick, Paul W.: Propulsion Influences on Air Combat. AIAA 85-1457, July 1985.

13. Gallaway, C. R.; and Osborn, R. F.: Aerodynamics Perspective of Supermaneuverability. AIAA 85-4068, Oct. 1985.

14. Berrier, Bobby L.; and Taylor, John G.: *Internal Performance of Two Nozzles Utilizing Gimbal Concepts for Thrust Vectoring.* NASA TP-2991, 1990.

15. Re, Richard J.; and Leavitt, Laurence D.: *Static Internal Performance Including Thrust Vectoring and Reversing of Two-Dimensional Convergent-Divergent Nozzles.* NASA TP-2253, 1984.

16. Capone, Francis J.; and Bare, E. Ann: *Multiaxis Control Power From Thrust Vectoring for a Supersonic Fighter Aircraft Model at Mach 0.20 to 2.47.* NASA TP-2712, 1987.

17. Capone, Francis J.; and Mason, Mary L.: *Multiaxis Aircraft Control Power From Thrust Vectoring at High Angles of Attack.* NASA TM-87741, 1986.

18. Bare, E. Ann; and Reubush, David E.: *Static Internal Performance of a Two-Dimensional Convergent-Divergent Nozzle With Thrust Vectoring.* NASA TP-2721, 1987.

19. Taylor, John G.: *Static Investigation of a Two-Dimensional Convergent-Divergent Exhaust Nozzle With Multiaxis Thrust Vectoring Capability.* NASA TP-2973, 1990.

20. Mason, Mary L.; and Berrier, Bobby L.: *Static Investigation of Several Yaw Vectoring Concepts on Nonaxisymmetric Nozzles.* NASA TP-2432, 1985.

21. Mason, Mary L.; and Berrier, Bobby L.: *Static Performance of Nonaxisymmetric Nozzles With Yaw Thrust-Vectoring Vanes.* NASA TP-2813, 1988.

22. Berrier, Bobby L.: Results from NASA Langley Experimental Studies of Multiaxis Thrust Vectoring Nozzles. *SAE 1988 Transactions—Journal of Aerospace,* Section 1—Volume 97, c.1989, pp. 1.1289–1.1304. (Available as SAE Paper 881481.)

23. Peddrew, Kathryn H., compiler: *A User's Guide to the Langley 16-Foot Transonic Tunnel.* NASA TM-83186, 1981.

24. Mercer, Charles E.; Berrier, Bobby L.; Capone, Francis J.; Grayston, Alan M.; and Sherman, C. D.: *Computations for the 16-Foot Transonic Tunnel—NASA Langley Research Center, Revision 1.* NASA TM-86319, 1987. (Supersedes NASA TM-86319, 1984.)

25. Shapiro, Ascher H.: *The Dynamics and Thermodynamics of Compressible Fluid Flow, Volume I.* Ronald Press Co., c.1953.

Table 1. Static Pressure Orifice Locations for Dry Power Subsonic Cruise Configurations

(a) Static pressure orifices in top view with $w_t = 3.05$ in.

Values of $\frac{y}{w_t/2}$ at—			
$x/L = 0$	$x/L = 0.262$	$x/L = 0.525$	$x/L = 0.803$
−0.604			
−.490			
−.381			
−.280			
−.191			
−.117			
−.007			
.104	0.104	0.104	0.104
.191	.191	.191	.191
.295	.295	.295	.295
.469	.469	.469	.469
.712	.712	.712	.712
.921	.921	.921	.921

(b) Static pressure orifices in side view with $h_t = 1.31$ in.

Values of $\frac{z}{h_t/2}$ at—	
$x/L = 0$	$x/L = 0.916$
−0.558	
−.456	
−.360	
−.131	
.105	0.105
.192	.192
.296	.296
.470	.470
.714	.714
.923	.923

Table 2. Static Pressure Orifice Locations for Dry Power
Supersonic Cruise Configurations

(a) Static pressure orifices in top view with $w_t = 3.05$ in.

Values of $\frac{y}{w_t/2}$ at—			
$x/L = 0$	$x/L = 0.262$	$x/L = 0.525$	$x/L = 0.803$
−0.604			
−.490			
−.381			
−.280			
−.191			
−.117			
−.007			
.102	0.102	0.102	0.102
.187	.187	.187	.187
.289	.289	.289	.289
.459	.459	.459	.459
.697	.697	.697	.697
.900	.900	.900	.900

(b) Static pressure orifices in side view
with $h_t = 1.31$ in.

Values of $\frac{z}{h_t/2}$ at—	
$x/L = 0$	$x/L = 0.916$
−0.558	
−.456	
−.360	
−.131	
.105	0.105
.192	.192
.296	.296
.470	.470
.714	.714
.923	.923

Table 3. Static Pressure Orifice Locations for Maximum Afterburning Power Configurations

(a) Static pressure orifices in top view with $w_t = 3.05$ in.

Values of $\frac{y}{w_t/2}$ at—			
$x/L = 0$	$x/L = 0.262$	$x/L = 0.525$	$x/L = 0.803$
−0.499			
−.385			
−.276			
−.176			
−.087			
−.007			
.104	0.104	0.104	0.104
.191	.191	.191	.191
.295	.295	.295	.295
.469	.469	.469	.469
.712	.712	.712	.712
.921	.921	.921	.921

(b) Static pressure orifices in side view
with $h_t = 2.29$ in.

Values of $\frac{z}{h_t/2}$ at—	
$x/L = 0$	$x/L = 0.524$
−0.453	
−.352	
−.255	
−.077	
.105	0.105
.192	.192
.296	.296
.470	.470
.714	.714
.923	.923

Table 4. Static Pressure Ratios for 18° Dry Power Subsonic Cruise Configuration

(a) Orifices located on nozzle centerline and divergent flap

NPR	$y/(w_t/2) = 0$ x/L												
	-.604	-.490	-.381	-.280	-.191	-.117	-.007	.104	.191	.295	.469	.712	.921
1.821	.985	.983	.984	.983	.973	.960	.383	.369	.389	.408	.434	.478	.515
1.999	.987	.984	.987	.983	.974	.958	.370	.311	.330	.346	.382	.432	.475
2.512	.986	.982	.987	.985	.974	.959	.307	.253	.227	.210	.179	.258	.371
3.005	.986	.985	.987	.983	.974	.957	.305	.249	.225	.209	.179	.180	.304
3.504	.985	.985	.988	.983	.974	.959	.300	.246	.223	.209	.179	.180	.235
4.014	.985	.985	.988	.983	.975	.959	.292	.244	.223	.208	.179	.180	.233
5.015	.985	.985	.988	.983	.975	.958	.289	.241	.223	.209	.179	.177	.231
6.018	.985	.986	.988	.983	.975	.959	.290	.241	.225	.210	.179	.176	.230
7.007	.985	.986	.987	.983	.975	.958	.286	.242	.228	.212	.180	.175	.229
8.014	.985	.985	.987	.982	.975	.959	.276	.242	.229	.212	.180	.174	.229
10.031	.985	.986	.987	.982	.974	.958	.262	.244	.227	.209	.179	.174	.229
10.999	.985	.986	.987	.982	.974	.958	.257	.244	.227	.209	.179	.175	.229

NPR	$x/L = 0.104$ $y/(w_t/2)$				$x/L = 0.191$ $y/(w_t/2)$				$x/L = 0.295$ $y/(w_t/2)$			
	.000	.262	.525	.803	.000	.262	.525	.803	.000	.262	.525	.803
1.821	.369	.349	.290	.513	.389	.374	.332	.467	.408	.395	.377	.438
1.999	.311	.304	.264	.498	.330	.321	.316	.434	.346	.337	.356	.395
2.512	.253	.204	.221	.467	.227	.225	.303	.400	.210	.223	.356	.310
3.005	.249	.200	.220	.465	.225	.225	.307	.399	.209	.224	.358	.307
3.504	.246	.198	.219	.462	.223	.225	.307	.397	.209	.226	.356	.306
4.014	.244	.197	.219	.462	.223	.225	.308	.397	.208	.227	.356	.305
5.015	.241	.196	.220	.460	.223	.224	.307	.396	.209	.226	.351	.303
6.018	.241	.201	.222	.459	.225	.222	.301	.395	.210	.220	.342	.302
7.007	.242	.214	.222	.461	.228	.220	.289	.395	.212	.212	.323	.302
8.014	.242	.221	.222	.463	.229	.217	.284	.396	.212	.205	.319	.301
10.031	.244	.218	.223	.464	.227	.211	.287	.397	.209	.198	.325	.302
10.999	.244	.217	.224	.463	.227	.212	.288	.397	.209	.199	.326	.302

NPR	$x/L = 0.469$ $y/(w_t/2)$				$x/L = 0.712$ $y/(w_t/2)$				$x/L = 0.921$ $y/w_t/2$			
	.000	.262	.525	.803	.000	.262	.525	.803	.000	.262	.525	.803
1.821	.434	.420	.458	.484	.478	.478	.502	.514	.515	.519	.537	.543
1.999	.382	.370	.416	.455	.432	.429	.454	.453	.475	.477	.493	.491
2.512	.179	.171	.254	.285	.258	.198	.193	.208	.371	.381	.355	.399
3.005	.179	.173	.254	.283	.180	.162	.191	.208	.304	.303	.306	.301
3.504	.179	.174	.254	.282	.180	.163	.191	.209	.235	.226	.164	.158
4.014	.179	.174	.254	.282	.180	.163	.191	.209	.233	.218	.152	.157
5.015	.179	.174	.253	.280	.177	.164	.191	.208	.231	.209	.153	.157
6.018	.179	.171	.248	.277	.176	.162	.189	.206	.230	.212	.152	.157
7.007	.180	.165	.242	.273	.175	.159	.188	.201	.229	.220	.152	.157
8.014	.180	.160	.241	.270	.174	.159	.185	.199	.229	.226	.152	.155
10.031	.179	.154	.237	.268	.174	.159	.182	.196	.229	.233	.153	.154
10.999	.179	.155	.237	.269	.175	.159	.183	.197	.229	.231	.153	.154

Table 4. Concluded

(b) Orifices located on nozzle sidewall and convergent flap lip

NPR	$z/(h_t/2) = 0$									
	x/L									
	-.558	-.456	-.360	-.131	.105	.192	.296	.470	.714	.923
1.821	.983	.972	.953	.637	.489	.476	.441	.484	.509	.539
1.999	.982	.973	.951	.632	.380	.466	.419	.474	.446	.488
2.512	.983	.970	.950	.630	.341	.385	.365	.287	.277	.376
3.005	.982	.973	.952	.631	.339	.383	.362	.286	.212	.308
3.504	.982	.974	.952	.631	.339	.383	.362	.285	.212	.183
4.014	.982	.974	.952	.633	.339	.385	.361	.285	.212	.161
5.015	.982	.974	.951	.633	.338	.385	.359	.284	.211	.160
6.018	.981	.976	.952	.633	.337	.386	.358	.282	.210	.160
7.007	.981	.976	.952	.633	.338	.392	.356	.279	.208	.160
8.014	.981	.975	.950	.633	.336	.395	.357	.278	.206	.160
10.031	.980	.976	.950	.633	.335	.393	.357	.278	.205	.161
10.999	.980	.977	.950	.633	.336	.391	.355	.277	.205	.161

NPR	$z/(h_t/2) = 0.916$					
	x/L					
	.105	.192	.296	.470	.714	.923
1.821	.550	.476	.459	.482	.509	.541
1.999	.538	.444	.425	.466	.442	.491
2.512	.510	.400	.336	.286	.208	.375
3.005	.509	.397	.333	.284	.207	.304
3.504	.509	.396	.333	.283	.207	.160
4.014	.509	.396	.332	.282	.208	.160
5.015	.509	.393	.331	.280	.207	.160
6.018	.511	.392	.330	.277	.204	.159
7.007	.515	.393	.328	.272	.199	.159
8.014	.517	.396	.330	.270	.196	.157
10.031	.517	.399	.331	.268	.194	.157
10.999	.516	.398	.330	.268	.195	.157

NPR	ϕ, deg		
	0	33	66
1.821	.383	.860	.889
1.999	.370	.863	.888
2.512	.307	.859	.887
3.005	.305	.861	.889
3.504	.300	.861	.889
4.014	.292	.862	.889
5.015	.289	.859	.888
6.018	.290	.861	.888
7.007	.286	.860	.888
8.014	.276	.860	.887
10.031	.262	.860	.887
10.999	.257	.860	.887

Table 5. Static Pressure Ratios for 0° Dry Power Subsonic Cruise Configuration

(a) Orifices located on nozzle centerline and divergent flap

NPR	$y/(w_t/2) = 0$ x/L												
	-.604	-.490	-.381	-.280	-.191	-.117	-.007	.104	.191	.295	.469	.712	.921
1.806	.980	.978	.980	.975	.966	.946	.236	.269	.290	.293	.326	.493	.543
2.002	.979	.979	.981	.976	.970	.946	.234	.269	.287	.291	.264	.444	.506
2.511	.979	.977	.981	.976	.970	.948	.239	.264	.280	.288	.262	.288	.327
3.002	.980	.980	.982	.976	.969	.949	.235	.260	.276	.285	.262	.288	.234
3.507	.980	.981	.982	.978	.969	.949	.234	.256	.273	.283	.261	.288	.234
4.005	.980	.981	.982	.977	.969	.949	.233	.254	.271	.282	.261	.288	.234
5.008	.981	.980	.983	.978	.970	.949	.226	.250	.269	.282	.261	.287	.233
6.012	.980	.981	.983	.978	.969	.950	.221	.246	.269	.285	.261	.288	.233
7.010	.980	.981	.983	.978	.970	.950	.220	.242	.274	.287	.260	.288	.232
8.006	.980	.980	.983	.978	.969	.949	.220	.244	.275	.288	.260	.287	.232
10.004	.980	.981	.983	.978	.970	.949	.215	.244	.275	.290	.261	.286	.231
11.003	.980	.981	.982	.977	.970	.950	.218	.243	.273	.289	.261	.295	.229

NPR	x/L = 0.104 $y/(w_t/2)$				x/L = 0.191 $y/(w_t/2)$				x/L = 0.295 $y/(w_t/2)$			
	.000	.262	.525	.803	.000	.262	.525	.803	.000	.262	.525	.803
1.806	.269	.254	.439	.451	.290	.329	.401	.407	.293	.328	.339	.336
2.002	.269	.254	.440	.449	.287	.329	.401	.407	.291	.327	.339	.333
2.511	.264	.250	.439	.446	.280	.324	.399	.406	.288	.324	.337	.332
3.002	.260	.249	.436	.445	.276	.322	.396	.405	.285	.323	.336	.329
3.507	.256	.245	.434	.445	.273	.319	.392	.406	.283	.320	.333	.327
4.005	.254	.247	.440	.445	.271	.321	.392	.406	.282	.318	.332	.327
5.008	.250	.250	.436	.442	.269	.326	.390	.406	.282	.316	.331	.325
6.012	.246	.249	.433	.442	.269	.331	.389	.405	.285	.314	.330	.325
7.010	.242	.243	.421	.446	.274	.329	.381	.405	.287	.316	.326	.323
8.006	.244	.243	.414	.444	.275	.338	.380	.404	.288	.320	.326	.322
10.004	.244	.254	.414	.443	.275	.354	.386	.402	.290	.322	.329	.323
11.003	.243	.254	.417	.442	.273	.354	.387	.400	.289	.319	.327	.322

NPR	x/L = 0.469 $y/(w_t/2)$				x/L = 0.712 $y/(w_t/2)$				x/L = 0.921 $y/(w_t/2)$			
	.000	.262	.525	.803	.000	.262	.525	.803	.000	.262	.525	.803
1.806	.326	.254	.250	.283	.493	.497	.490	.494	.543	.548	.550	.538
2.002	.264	.246	.248	.276	.444	.432	.428	.451	.506	.509	.516	.489
2.511	.262	.244	.245	.270	.288	.244	.214	.212	.327	.316	.361	.379
3.002	.262	.244	.243	.268	.288	.245	.214	.211	.234	.230	.233	.274
3.507	.261	.244	.242	.264	.288	.247	.215	.210	.234	.228	.230	.178
4.005	.261	.244	.241	.264	.288	.247	.213	.209	.234	.228	.230	.178
5.008	.261	.244	.239	.262	.287	.246	.212	.208	.233	.227	.229	.178
6.012	.261	.243	.238	.262	.288	.242	.211	.208	.233	.227	.230	.176
7.010	.260	.244	.239	.261	.288	.236	.210	.208	.232	.226	.230	.175
8.006	.260	.245	.239	.260	.287	.232	.209	.208	.232	.226	.230	.175
10.004	.261	.245	.247	.268	.286	.221	.206	.207	.231	.227	.231	.170
11.003	.261	.244	.241	.263	.285	.226	.208	.209	.229	.226	.230	.173

Table 5. Concluded

(b) Orifices located on nozzle sidewall and convergent flap lip

NPR	z/(h_t/2) = 0									
	x/L									
	-.558	-.456	-.360	-.131	.105	.192	.296	.470	.714	.923
1.806	.972	.961	.945	.726	.469	.378	.352	.330	.472	.520
2.002	.974	.962	.945	.728	.467	.378	.351	.291	.448	.473
2.511	.975	.962	.942	.725	.466	.375	.349	.289	.282	.376
3.002	.974	.964	.945	.728	.466	.374	.348	.288	.206	.305
3.507	.976	.965	.946	.730	.466	.372	.349	.286	.205	.172
4.005	.975	.966	.946	.729	.467	.370	.347	.286	.205	.171
5.008	.974	.965	.945	.728	.466	.368	.346	.284	.204	.170
6.012	.975	.967	.946	.728	.466	.368	.345	.284	.201	.169
7.010	.975	.967	.946	.728	.465	.368	.348	.282	.199	.169
8.006	.974	.966	.945	.727	.464	.367	.345	.282	.199	.169
10.004	.974	.967	.945	.726	.465	.369	.347	.281	.199	.168
11.003	.974	.968	.945	.728	.464	.367	.342	.282	.200	.168

NPR	z/(h_t/2) = 0.916					
	x/L					
	.105	.192	.296	.470	.714	.923
1.806	.464	.417	.355	.319	.476	.524
2.002	.463	.416	.355	.273	.446	.474
2.511	.461	.414	.355	.271	.252	.375
3.002	.460	.413	.355	.269	.207	.305
3.507	.461	.416	.355	.267	.205	.172
4.005	.461	.415	.356	.267	.204	.172
5.008	.460	.413	.355	.265	.203	.172
6.012	.461	.413	.355	.264	.202	.170
7.010	.463	.416	.354	.262	.202	.170
8.006	.462	.413	.353	.262	.202	.169
10.004	.462	.408	.351	.270	.202	.166
11.003	.462	.407	.350	.266	.203	.168
10.994	.462	.407	.350	.266	.203	.168

NPR	φ, deg		
	0	33	60
1.806	.236	.805	.896
2.002	.234	.804	.897
2.511	.239	.803	.891
3.002	.235	.801	.893
3.507	.234	.805	.894
4.005	.233	.805	.893
5.008	.226	.803	.893
6.012	.221	.803	.893
7.010	.220	.804	.892
8.006	.220	.803	.891
10.004	.215	.804	.892
11.003	.218	.803	.891
10.994	.219	.803	.891

Table 6. Static Pressure Ratios for −18° Dry Power Subsonic Cruise Configuration

(a) Orifices located on nozzle centerline and divergent flap

NPR	$y/(w_t/2) = 0$ x/L −.604	−.490	−.381	−.280	−.191	−.117	−.007	.104	.191	.295	.469	.712	.921
1.815	.976	.976	.979	.973	.968	.941	.183	.322	.384	.357	.263	.467	.541
2.017	.976	.979	.979	.973	.968	.942	.178	.321	.382	.356	.264	.394	.468
2.497	.979	.976	.981	.975	.967	.945	.165	.321	.380	.352	.263	.246	.336
3.015	.978	.979	.980	.974	.968	.943	.155	.319	.377	.351	.263	.246	.233
3.508	.979	.979	.981	.974	.967	.944	.151	.321	.377	.349	.263	.246	.233
4.003	.978	.980	.982	.975	.968	.944	.147	.325	.378	.349	.262	.244	.233
4.997	.979	.979	.981	.975	.968	.944	.144	.325	.378	.348	.261	.247	.232
5.999	.979	.980	.981	.981	.967	.944	.145	.332	.377	.348	.261	.247	.231
7.008	.979	.980	.981	.975	.967	.944	.146	.342	.378	.347	.261	.245	.231
8.004	.979	.979	.982	.975	.967	.944	.146	.354	.378	.346	.261	.242	.231
10.015	.979	.980	.981	.975	.967	.944	.149	.363	.378	.346	.262	.238	.231
11.026	.979	.980	.981	.975	.966	.944	.150	.370	.378	.345	.261	.234	.231

NPR	x/L = 0.104 $y/(w_t/2)$ .000	.262	.525	.803	x/L = 0.191 $y/(w_t/2)$ .000	.262	.525	.803	x/L = 0.295 $y/(w_t/2)$ .000	.262	.525	.803
1.815	.322	.328	.333	.344	.384	.389	.375	.399	.357	.350	.363	.340
2.017	.321	.327	.333	.342	.382	.388	.373	.398	.356	.349	.363	.339
2.497	.321	.324	.331	.338	.380	.387	.373	.397	.352	.348	.362	.336
3.015	.319	.323	.328	.336	.377	.387	.371	.395	.351	.345	.362	.333
3.508	.321	.321	.326	.335	.377	.387	.369	.395	.349	.345	.361	.331
4.003	.325	.320	.326	.336	.378	.386	.368	.395	.349	.344	.362	.331
4.997	.325	.319	.325	.336	.378	.386	.364	.392	.348	.343	.361	.328
5.999	.332	.316	.325	.339	.377	.388	.363	.391	.348	.344	.362	.328
7.008	.342	.313	.325	.340	.376	.388	.363	.391	.347	.344	.362	.327
8.004	.354	.310	.326	.340	.378	.389	.361	.392	.346	.344	.362	.326
10.015	.363	.309	.325	.346	.378	.392	.360	.392	.346	.346	.363	.326
11.026	.370	.307	.325	.347	.378	.395	.360	.392	.345	.346	.363	.326

NPR	x/L = 0.469 $y/(w_t/2)$ .000	.262	.525	.803	x/L = 0.712 $y/(w_t/2)$ .000	.262	.525	.803	x/L = 0.921 $y/(w_t/2)$ .000	.262	.525	.803
1.815	.263	.266	.257	.262	.467	.459	.448	.465	.541	.544	.548	.544
2.017	.264	.265	.255	.259	.394	.388	.384	.385	.468	.466	.459	.468
2.497	.263	.264	.253	.257	.246	.236	.248	.242	.336	.339	.356	.359
3.015	.263	.262	.253	.253	.246	.238	.247	.240	.233	.234	.226	.221
3.508	.263	.262	.252	.253	.246	.239	.247	.239	.233	.233	.226	.221
4.003	.262	.263	.252	.252	.244	.240	.248	.237	.233	.232	.225	.221
4.997	.261	.262	.250	.251	.247	.244	.249	.232	.232	.230	.223	.221
5.999	.261	.262	.250	.251	.247	.245	.249	.229	.231	.229	.224	.221
7.008	.261	.261	.249	.250	.245	.243	.249	.228	.231	.229	.224	.222
8.004	.261	.261	.250	.250	.242	.243	.249	.227	.231	.229	.223	.222
10.015	.262	.262	.250	.250	.238	.241	.249	.226	.231	.228	.223	.222
11.026	.261	.262	.249	.249	.234	.240	.248	.226	.231	.228	.223	.222

Table 6. Concluded

(b) Orifices located on nozzle sidewall and convergent flap lip

NPR	z/(h$_t$/2) = 0									
	x/L									
	-.558	-.456	-.360	-.131	.105	.192	.296	.470	.714	.923
1.815	.970	.961	.947	.787	.493	.348	.250	.287	.506	.543
2.017	.971	.958	.946	.788	.493	.350	.251	.286	.423	.486
2.497	.971	.959	.945	.784	.492	.350	.250	.284	.235	.374
3.015	.970	.961	.946	.787	.492	.349	.249	.281	.235	.233
3.508	.972	.963	.947	.789	.491	.349	.249	.280	.236	.187
4.003	.971	.963	.947	.789	.492	.349	.249	.279	.236	.186
4.997	.971	.963	.947	.787	.491	.349	.250	.277	.237	.187
5.999	.971	.964	.947	.787	.490	.349	.251	.276	.239	.186
7.008	.971	.964	.947	.788	.491	.348	.251	.276	.240	.186
8.004	.972	.964	.947	.787	.489	.348	.251	.275	.240	.186
10.015	.971	.965	.947	.787	.489	.348	.253	.275	.242	.186
11.026	.971	.965	.947	.786	.489	.348	.253	.274	.243	.186

NPR	z/(h$_t$/2) = 0.916					
	x/L					
	.105	.192	.296	.470	.714	.923
1.815	.383	.404	.353	.251	.475	.540
2.017	.383	.403	.353	.251	.407	.473
2.497	.382	.400	.352	.250	.220	.375
3.015	.381	.397	.350	.249	.219	.217
3.508	.382	.397	.350	.248	.219	.217
4.003	.382	.397	.349	.247	.219	.217
4.997	.381	.396	.349	.246	.214	.218
5.999	.380	.396	.349	.245	.212	.219
7.008	.380	.396	.348	.244	.212	.220
8.004	.381	.395	.349	.243	.212	.220
10.015	.382	.392	.349	.242	.211	.220
11.026	.384	.393	.348	.241	.211	.219

NPR	φ, deg		
	0	33	53
1.815	.183	.786	.914
2.017	.178	.785	.912
2.497	.165	.784	.911
3.015	.155	.782	.911
3.508	.151	.785	.912
4.003	.147	.785	.912
4.997	.144	.783	.910
5.999	.145	.782	.911
7.008	.146	.783	.910
8.004	.146	.782	.909
10.015	.149	.781	.909
11.026	.150	.781	.908

17

Table 7. Static Pressure Ratios for 18° Dry Power Supersonic Cruise Configuration

(a) Orifices located on nozzle centerline and divergent flap

| NPR | $y/(w_t/2) = 0$ | | | | | | | | | | | | |
| | x/L | | | | | | | | | | | | |
	-.604	-.490	-.381	-.280	-.191	-.117	*	.102	.187	.289	.459	.697	.900
1.810	.985	.980	.989	.982	.976	.959		.451	.451	.452	.466	.478	.490
2.011	.986	.983	.987	.982	.975	.957		.372	.371	.381	.401	.421	.438
2.507	.986	.979	.986	.982	.974	.957		.273	.280	.292	.316	.335	.347
3.012	.985	.983	.987	.981	.975	.957		.183	.175	.164	.188	.255	.297
3.510	.985	.983	.987	.982	.975	.958		.177	.166	.146	.127	.197	.233
3.998	.985	.983	.987	.981	.973	.958		.175	.164	.144	.124	.187	.205
4.997	.985	.983	.988	.982	.975	.957		.174	.160	.144	.125	.106	.168
5.999	.984	.984	.987	.982	.975	.958		.176	.158	.143	.126	.108	.102
7.007	.984	.984	.987	.982	.975	.958		.177	.156	.142	.126	.107	.089
8.006	.984	.985	.987	.982	.974	.958		.177	.156	.143	.126	.107	.089
10.006	.984	.985	.987	.981	.974	.958		.178	.156	.142	.125	.107	.089
11.019	.984	.985	.986	.981	.974	.958		.177	.156	.143	.125	.106	.089
12.101	.984	.985	.986	.981	.974	.958		.176	.156	.143	.125	.106	.088

* Data not available.

| NPR | x/L = 0.102 | | | | x/L = 0.187 | | | | x/L = 0.289 | | | |
| | $y/(w_t/2)$ | | | | $y/(w_t/2)$ | | | | $y/(w_t/2)$ | | | |
	.000	.262	.525	.803	.000	.262	.525	.803	.000	.262	.525	.803
1.810	.451	.439	.416	.462	.451	.442	.430	.478	.452	.454	.450	.486
2.011	.372	.356	.333	.436	.371	.361	.350	.421	.381	.380	.376	.423
2.507	.273	.260	.233	.423	.280	.270	.264	.362	.292	.293	.301	.314
3.012	.183	.128	.155	.391	.175	.163	.186	.319	.164	.174	.257	.253
3.510	.177	.124	.155	.390	.166	.159	.185	.318	.146	.168	.255	.251
3.998	.175	.122	.153	.390	.164	.159	.184	.317	.144	.171	.256	.250
4.997	.174	.125	.154	.390	.160	.157	.189	.317	.144	.168	.253	.249
5.999	.176	.126	.155	.390	.158	.158	.193	.318	.143	.164	.253	.249
7.007	.177	.125	.157	.390	.156	.157	.195	.318	.142	.162	.252	.250
8.006	.177	.123	.157	.391	.156	.157	.195	.318	.143	.162	.252	.250
10.006	.178	.120	.161	.392	.156	.152	.195	.319	.143	.155	.250	.251
11.019	.177	.120	.142	.392	.156	.150	.196	.320	.143	.153	.249	.252
12.101	.176	.120	.162	.393	.156	.150	.196	.320	.143	.152	.249	.251

| NPR | x/L = 0.459 | | | | x/L = 0.697 | | | | x/L = 0.900 | | | |
| | $y/(w_t/2)$ | | | | $y/(w_t/2)$ | | | | $y/(w_t/2)$ | | | |
	.000	.262	.525	.803	.000	.262	.525	.803	.000	.262	.525	.803
1.810	.466	.462	.465	.489	.478	.476	.482	.503	.490	.485	.491	.519
2.011	.401	.397	.401	.440	.421	.420	.428	.452	.438	.435	.446	.471
2.507	.316	.314	.326	.330	.335	.335	.342	.356	.347	.345	.357	.371
3.012	.188	.161	.196	.182	.255	.259	.257	.254	.297	.303	.336	.324
3.510	.127	.125	.186	.178	.197	.191	.115	.171	.233	.232	.260	.284
3.998	.124	.128	.186	.175	.187	.163	.117	.119	.205	.205	.208	.214
4.997	.125	.126	.184	.176	.106	.087	.111	.119	.168	.176	.180	.175
5.999	.126	.121	.183	.176	.108	.085	.109	.120	.102	.075	.080	.087
7.007	.126	.120	.182	.176	.107	.085	.108	.119	.089	.074	.078	.086
8.006	.126	.120	.181	.175	.107	.085	.108	.119	.089	.073	.078	.086
10.006	.125	.116	.180	.176	.107	.084	.106	.118	.089	.073	.077	.086
11.019	.125	.115	.179	.176	.106	.084	.105	.117	.089	.073	.077	.085
12.101	.125	.115	.179	.176	.106	.084	.105	.117	.088	.073	.076	.085

Table 7. Concluded

(b) Orifices located on nozzle sidewall and convergent flap lip

NPR	z/(h_t/2) = 0									
	x/L									
	-.558	-.456	-.360	-.131	.105	.192	.296	.470	.714	.923
1.810	.981	.970	.956	.665	.486	.441	.437	.495	.517	.546
2.011	.980	.970	.953	.647	.462	.410	.364	.509	.432	.482
2.507	.981	.969	.951	.634	.375	.358	.313	.256	.445	.330
3.012	.980	.971	.952	.632	.340	.283	.246	.184	.283	.310
3.510	.981	.973	.953	.633	.340	.282	.244	.183	.259	.271
3.998	.981	.973	.951	.635	.339	.282	.243	.183	.125	.236
4.997	.981	.974	.951	.634	.339	.280	.241	.181	.124	.151
5.999	.980	.974	.951	.633	.338	.280	.242	.180	.124	.098
7.007	.980	.975	.951	.633	.338	.280	.241	.178	.123	.098
8.006	.980	.975	.950	.633	.337	.280	.241	.178	.122	.098
10.006	.980	.976	.950	.633	.338	.279	.241	.178	.121	.097
11.019	.980	.976	.950	.633	.337	.279	.241	.177	.120	.097
12.101	.980	.977	.950	.633	.337	.279	.241	.179	.120	.097

NPR	z/(h_t/2) = 0.916					
	x/L					
	.105	.192	.296	.470	.714	.923
1.810	.491	.420	.429	.469	.513	.546
2.011	.458	.399	.379	.480	.449	.475
2.507	.438	.369	.317	.294	.405	.366
3.012	.386	.315	.255	.192	.275	.325
3.510	.386	.314	.254	.181	.255	.270
3.998	.387	.313	.254	.181	.127	.235
4.997	.388	.313	.253	.180	.125	.156
5.999	.389	.313	.253	.179	.124	.096
7.007	.389	.312	.253	.179	.123	.095
8.006	.389	.312	.252	.179	.122	.095
10.006	.388	.311	.252	.178	.122	.095
11.019	.388	.311	.252	.178	.122	.095
12.101	.388	.311	.252	.177	.122	.095

NPR	φ, deg		
	*	33	66
1.810		.862	.894
2.011		.859	.889
2.507		.857	.887
3.012		.858	.890
3.510		.858	.890
3.998		.858	.889
4.997		.857	.888
5.999		.858	.888
7.007		.857	.888
8.006		.857	.887
10.006		.857	.887
11.019		.857	.886
12.101		.857	.887

* Data not available.

Table 8. Static Pressure Ratios for 0° Dry Power Supersonic Cruise Configuration

(a) Orifices located on nozzle centerline and divergent flap

NPR	$y/(w_t/2) = 0$, x/L												
	-.604	-.490	-.381	-.280	-.191	-.117	-.007	.102	.187	.289	.459	.697	.900
1.805	.981	.980	.983	.980	.971	.953	.481	.347	.343	.363	.409	.495	.549
1.999	.979	.977	.982	.978	.971	.950	.428	.249	.265	.307	.360	.439	.495
2.519	.981	.979	.982	.979	.971	.952	.127	.161	.203	.205	.207	.383	.424
3.000	.980	.979	.983	.977	.970	.950	.127	.159	.199	.203	.197	.255	.335
3.508	.980	.980	.983	.978	.970	.950	.117	.159	.197	.202	.196	.147	.248
4.008	.981	.980	.984	.977	.970	.950	.106	.158	.195	.201	.196	.146	.224
5.000	.981	.980	.984	.979	.971	.949	.099	.155	.190	.201	.195	.146	.107
6.001	.981	.981	.984	.978	.970	.950	.101	.151	.187	.200	.194	.144	.107
7.005	.981	.981	.983	.978	.970	.950	.088	.145	.185	.201	.193	.143	.106
7.998	.981	.980	.983	.978	.970	.950	.100	.139	.185	.203	.192	.141	.105
10.010	.981	.981	.983	.978	.970	.950	.099	.135	.185	.203	.188	.139	.103
11.006	.981	.981	.983	.977	.969	.949	.107	.134	.185	.201	.186	.137	.102

NPR	x/L = 0.102, $y/(w_t/2)$				x/L = 0.187, $y/(w_t/2)$				x/L = 0.289, $y/(w_t/2)$			
	.000	.262	.525	.803	.000	.262	.525	.803	.000	.262	.525	.803
1.805	.347	.337	.380	.357	.343	.338	.365	.394	.363	.367	.392	.372
1.999	.249	.247	.362	.311	.265	.268	.315	.352	.307	.323	.301	.309
2.519	.161	.162	.303	.290	.203	.220	.278	.302	.205	.245	.251	.263
3.000	.159	.161	.302	.288	.199	.220	.277	.300	.203	.246	.251	.262
3.508	.159	.158	.299	.288	.197	.224	.278	.299	.202	.245	.250	.261
4.008	.158	.155	.297	.286	.195	.225	.277	.299	.201	.245	.249	.260
5.000	.155	.153	.293	.285	.190	.232	.275	.298	.201	.243	.247	.258
6.001	.151	.152	.291	.286	.187	.236	.274	.298	.200	.241	.246	.258
7.005	.145	.150	.288	.286	.185	.240	.275	.298	.201	.239	.244	.257
7.998	.139	.150	.284	.286	.185	.239	.276	.297	.203	.237	.242	.258
10.010	.135	.151	.281	.289	.185	.235	.276	.297	.203	.236	.239	.258
11.006	.134	.149	.282	.291	.185	.232	.276	.297	.201	.236	.237	.258

NPR	x/L = 0.459, $y/(w_t/2)$				x/L = 0.697, $y/(w_t/2)$				x/L = 0.900, $y/(w_t/2)$			
	.000	.262	.525	.803	.000	.262	.525	.803	.000	.262	.525	.803
1.805	.409	.414	.449	.497	.495	.499	.519	.528	.549	.550	.559	.556
1.999	.360	.359	.410	.411	.439	.449	.470	.485	.495	.501	.506	.506
2.519	.207	.181	.192	.231	.383	.364	.412	.383	.424	.438	.456	.390
3.000	.197	.180	.191	.196	.255	.189	.182	.278	.335	.328	.422	.379
3.508	.196	.178	.191	.194	.147	.130	.122	.143	.248	.238	.220	.273
4.008	.196	.178	.190	.193	.146	.130	.122	.122	.224	.220	.210	.220
5.000	.195	.176	.190	.192	.146	.130	.120	.122	.107	.112	.173	.172
6.001	.194	.176	.189	.192	.144	.131	.120	.121	.107	.100	.090	.084
7.005	.193	.176	.187	.191	.143	.131	.119	.121	.106	.101	.090	.084
7.998	.192	.176	.185	.191	.141	.131	.119	.120	.105	.099	.090	.083
10.010	.188	.176	.184	.190	.139	.131	.119	.120	.103	.099	.090	.083
11.006	.186	.176	.184	.190	.137	.130	.118	.119	.102	.100	.090	.083

Table 8. Concluded

(b) Orifices located on nozzle sidewall and convergent flap lip

NPR	z/(h$_t$/2) = 0									
	x/L									
	-.558	-.456	-.360	-.131	.105	.192	.296	.470	.714	.923
1.805	.977	.965	.949	.748	.489	.371	.382	.537	.520	.543
1.999	.975	.964	.945	.738	.477	.356	.254	.433	.464	.492
2.519	.975	.962	.944	.729	.463	.340	.223	.366	.371	.366
3.000	.975	.965	.946	.729	.462	.340	.223	.292	.309	.309
3.508	.974	.965	.946	.731	.463	.340	.223	.155	.258	.269
4.008	.976	.966	.947	.730	.463	.340	.222	.155	.125	.233
5.000	.975	.965	.945	.728	.462	.341	.221	.153	.125	.152
6.001	.975	.966	.946	.727	.461	.341	.220	.152	.125	.100
7.005	.975	.966	.946	.728	.461	.341	.220	.151	.124	.098
7.998	.975	.966	.945	.727	.460	.341	.219	.150	.124	.098
10.010	.974	.967	.945	.726	.461	.341	.219	.148	.123	.097
11.006	.974	.967	.945	.726	.460	.341	.219	.148	.123	.097

NPR	z/(h$_t$/2) = 0.916					
	x/L					
	.105	.192	.296	.470	.714	.923
1.805	.412	.535	.496	.523	.506	.524
1.999	.318	.454	.438	.456	.456	.470
2.519	.292	.302	.260	.363	.365	.365
3.000	.290	.302	.258	.201	.305	.310
3.508	.288	.298	.258	.184	.259	.269
4.008	.286	.298	.258	.184	.122	.233
5.000	.281	.295	.258	.183	.116	.172
6.001	.276	.288	.258	.182	.116	.092
7.005	.273	.285	.257	.182	.114	.091
7.998	.271	.277	.257	.182	.115	.091
10.010	.268	.278	.256	.182	.114	.091
11.006	.267	.278	.257	.181	.115	.091

NPR	ϕ, deg		
	0	33	60
1.805	.481	.810	.899
1.999	.428	.806	.898
2.519	.127	.802	.894
3.000	.127	.801	.894
3.508	.117	.804	.893
4.008	.106	.804	.893
5.000	.099	.803	.892
6.001	.101	.803	.893
7.005	.088	.803	.892
7.998	.100	.803	.891
10.010	.099	.804	.891
11.006	.107	.803	.890

Table 9. Static Pressure Ratios for −18° Dry Power Supersonic Cruise Configuration

(a) Orifices located on nozzle centerline and divergent flap

NPR	$y/(w_t/2) = 0$												
	x/L												
	−.604	−.490	−.381	−.280	−.191	−.117	−.007	.102	.187	.289	.459	.697	.900
1.806	.977	.977	.982	.977	.967	.946	.448	.231	.290	.290	.468	.555	.560
2.016	.977	.976	.979	.974	.967	.944	.142	.217	.274	.260	.406	.500	.510
2.498	.979	.974	.979	.977	.965	.945	.143	.221	.275	.254	.203	.374	.426
2.999	.978	.979	.980	.976	.967	.945	.141	.226	.275	.253	.202	.262	.317
3.499	.977	.978	.982	.976	.967	.945	.140	.230	.275	.251	.202	.144	.263
4.007	.979	.979	.981	.976	.967	.944	.140	.234	.275	.252	.203	.141	.227
5.005	.979	.979	.982	.977	.968	.944	.139	.238	.277	.251	.202	.141	.103
6.020	.979	.980	.982	.976	.969	.945	.140	.242	.278	.250	.202	.141	.102
7.007	.978	.979	.981	.976	.967	.944	.141	.241	.278	.250	.202	.140	.102
8.002	.979	.979	.982	.976	.966	.944	.139	.241	.278	.249	.202	.140	.102
10.035	.978	.979	.981	.975	.966	.944	.139	.240	.279	.249	.202	.140	.102
10.939	.979	.980	.981	.975	.967	.944	.139	.241	.279	.249	.202	.140	.101

NPR	x/L = 0.102				x/L = 0.187				x/L = 0.289			
	$y/(w_t/2)$				$y/(w_t/2)$				$y/(w_t/2)$			
	.000	.262	.525	.803	.000	.262	.525	.803	.000	.262	.525	.803
1.806	.231	.207	.226	.230	.290	.264	.262	.299	.290	.284	.280	.296
2.016	.217	.196	.221	.227	.274	.240	.249	.294	.260	.262	.261	.384
2.498	.221	.194	.222	.226	.275	.237	.248	.288	.254	.262	.258	.260
2.999	.226	.194	.222	.225	.275	.237	.248	.288	.253	.263	.257	.260
3.499	.230	.193	.222	.223	.275	.236	.249	.286	.251	.264	.257	.259
4.007	.234	.192	.222	.222	.275	.235	.249	.285	.252	.264	.256	.259
5.005	.238	.190	.221	.220	.277	.233	.248	.284	.251	.263	.255	.258
6.020	.242	.189	.220	.220	.278	.232	.248	.284	.250	.264	.254	.258
7.007	.241	.189	.219	.219	.278	.231	.247	.283	.250	.264	.253	.257
8.002	.241	.188	.218	.219	.278	.230	.247	.283	.249	.264	.252	.258
10.035	.240	.188	.217	.219	.279	.231	.247	.283	.249	.264	.251	.262
10.939	.241	.188	.216	.219	.279	.231	.247	.284	.249	.264	.251	.261

NPR	x/L = 0.459				x/L = 0.697				x/L = 0.900			
	$y/(w_t/2)$				$y/(w_t/2)$				$y/(w_t/2)$			
	.000	.262	.525	.803	.000	.262	.525	.803	.000	.262	.525	.803
1.806	.468	.475	.461	.460	.555	.555	.558	.545	.560	.559	.560	.560
2.016	.406	.426	.441	.458	.500	.502	.492	.465	.510	.510	.496	.479
2.498	.203	.206	.208	.330	.374	.390	.448	.389	.426	.446	.427	.389
2.999	.202	.206	.207	.203	.262	.242	.227	.305	.317	.323	.405	.327
3.499	.202	.205	.208	.201	.144	.137	.136	.174	.263	.256	.251	.285
4.007	.203	.205	.207	.201	.141	.136	.136	.132	.227	.225	.225	.219
5.005	.202	.204	.207	.200	.141	.136	.135	.132	.103	.102	.119	.133
6.020	.202	.204	.206	.199	.141	.136	.135	.132	.102	.101	.096	.096
7.007	.202	.203	.206	.198	.140	.137	.134	.132	.102	.100	.096	.095
8.002	.202	.203	.206	.198	.140	.136	.134	.132	.102	.100	.096	.095
10.035	.202	.202	.206	.197	.140	.136	.133	.132	.102	.099	.096	.095
10.939	.202	.202	.205	.197	.140	.136	.133	.132	.101	.099	.096	.095

Table 9. Concluded

(b) Orifices located on nozzle sidewall and convergent flap lip

NPR	z/(h_t/2) = 0 x/L									
	-.558	-.456	-.360	-.131	.105	.192	.296	.470	.714	.923
1.806	.968	.962	.948	.785	.485	.351	.230	.423	.535	.544
2.016	.970	.960	.949	.783	.481	.348	.434	.453	.457	.462
2.498	.970	.960	.945	.781	.480	.348	.225	.371	.374	.366
2.999	.970	.964	.948	.781	.480	.348	.225	.309	.311	.303
3.499	.971	.963	.948	.783	.479	.347	.225	.238	.260	.258
4.007	.972	.963	.948	.785	.479	.348	.224	.122	.151	.229
5.005	.971	.963	.947	.783	.479	.349	.233	.122	.126	.120
6.020	.972	.965	.948	.783	.478	.353	.232	.122	.125	.113
7.007	.972	.964	.947	.784	.477	.353	.232	.121	.125	.113
8.002	.972	.964	.946	.783	.477	.353	.232	.121	.124	.113
10.035	.971	.965	.947	.783	.476	.353	.231	.121	.123	.112
10.939	.972	.965	.947	.783	.476	.354	.231	.121	.123	.112

NPR	z/(h_t/2) = 0.916 x/L					
	.105	.192	.296	.470	.714	.923
1.806	.254	.373	.445	.513	.506	.525
2.016	.246	.304	.439	.450	.451	.463
2.498	.242	.264	.254	.371	.369	.366
2.999	.241	.264	.247	.297	.306	.304
3.499	.240	.262	.247	.187	.253	.261
4.007	.239	.262	.246	.186	.121	.232
5.005	.238	.261	.246	.186	.120	.146
6.020	.237	.260	.246	.185	.120	.096
7.007	.237	.260	.246	.187	.120	.096
8.002	.236	.259	.245	.187	.119	.096
10.035	.236	.258	.245	.186	.119	.096
10.939	.236	.257	.245	.186	.119	.096

NPR	φ, deg		
	0	33	53
1.806	.448	.782	.912
2.016	.142	.782	.910
2.498	.143	.780	.909
2.999	.141	.779	.910
3.499	.140	.781	.910
4.007	.140	.782	.910
5.005	.139	.779	.909
6.020	.140	.779	.910
7.007	.141	.779	.909
8.002	.139	.778	.908
10.035	.139	.779	.908
10.939	.139	.779	.908

Table 10. Static Pressure Ratios for Maximum 35° A/B Configuration

(a) Orifices located on nozzle centerline and divergent flap

NPR	$y/(w_t/2) = 0$ x/L											
	-.499	-.385	-.276	-.176	-.087	-.007	.104	.191	.295	.469	.712	.921
1.810	.949	.945	.947	.944	.878	.392	.378	.404	.424	.449	.489	.523
1.999	.950	.945	.944	.944	.873	.316	.320	.354	.375	.403	.437	.470
2.503	.949	.945	.947	.943	.874	.151	.275	.300	.295	.265	.248	.347
3.002	.949	.948	.946	.943	.874	.148	.272	.298	.293	.264	.237	.262
3.501	.948	.948	.946	.942	.874	.145	.276	.287	.292	.265	.235	.218
3.806	.948	.948	.946	.941	.874	.141	.278	.288	.293	.265	.236	.216
3.996	.949	.948	.946	.942	.875	.143	.278	.282	.291	.264	.234	.214
5.002	.948	.948	.945	.940	.872	.152	.276	.277	.290	.264	.232	.212
5.999	.948	.949	.946	.941	.873	.144	.274	.274	.289	.264	.229	.209
7.004	.948	.949	.946	.941	.873	.134	.276	.270	.285	.263	.227	.206
7.795	.947	.948	.946	.940	.872	.147	.275	.272	.286	.262	.226	.205

NPR	x/L = 0.104 $y/(w_t/2)$				x/L = 0.191 $y/(w_t/2)$				x/L = 0.295 $y/(w_t/2)$			
	.000	.262	.525	.803	.000	.262	.525	.803	.000	.262	.525	.803
1.810	.378	.380	.374	.337	.404	.385	.411	.431	.424	.416	.398	.504
1.999	.320	.339	.329	.295	.354	.346	.354	.410	.375	.368	.329	.479
2.503	.275	.256	.232	.350	.300	.265	.217	.548	.295	.262	.241	.463
3.002	.272	.251	.225	.362	.298	.262	.217	.546	.293	.261	.241	.462
3.501	.276	.233	.196	.439	.287	.242	.206	.546	.292	.255	.240	.453
3.806	.278	.230	.193	.446	.288	.240	.205	.547	.293	.256	.241	.453
3.996	.278	.221	.181	.471	.282	.233	.200	.547	.291	.254	.240	.449
5.002	.276	.213	.171	.491	.277	.227	.195	.545	.290	.252	.237	.445
5.999	.274	.209	.169	.499	.274	.224	.194	.544	.289	.251	.235	.442
7.004	.276	.211	.166	.510	.270	.222	.191	.541	.285	.247	.233	.441
7.795	.275	.212	.165	.510	.272	.221	.190	.541	.286	.245	.231	.441

NPR	x/L = 0.469 $y/(w_t/2)$				x/L = 0.712 $y/(w_t/2)$				x/L = 0.921 $y/(w_t/2)$			
	.000	.262	.525	.803	.000	.262	.525	.803	.000	.262	.525	.803
1.810	.449	.450	.435	.529	.489	.487	.493	.537	.523	.522	.534	.551
1.999	.403	.398	.377	.456	.437	.436	.444	.491	.470	.468	.480	.496
2.503	.265	.240	.326	.366	.248	.218	.264	.273	.347	.357	.369	.368
3.002	.264	.240	.327	.365	.237	.217	.263	.273	.262	.198	.203	.196
3.501	.265	.238	.341	.359	.235	.220	.266	.274	.218	.193	.204	.199
3.806	.265	.239	.342	.360	.236	.219	.266	.275	.216	.191	.204	.200
3.996	.264	.239	.348	.357	.234	.221	.266	.275	.214	.192	.205	.201
5.002	.264	.236	.352	.354	.232	.222	.266	.276	.212	.192	.205	.201
5.999	.264	.236	.353	.352	.229	.223	.266	.277	.209	.192	.205	.201
7.004	.263	.233	.355	.351	.227	.225	.265	.277	.206	.193	.205	.201
7.795	.262	.232	.355	.350	.226	.224	.265	.277	.205	.193	.204	.200

Table 10. Concluded

(b) Orifices located on nozzle sidewall and convergent flap lip

NPR	$z/(h_t/2) = 0$									
	x/L									
	-.453	-.352	-.255	-.077	.105	.192	.296	.470	.714	.923
1.810	.939	.920	.885	.477	.505	.441	.393	.535	.517	.543
1.999	.938	.919	.884	.458	.487	.423	.361	.345	.522	.464
2.503	.940	.919	.894	.439	.456	.381	.309	.280	.256	.342
3.002	.939	.920	.885	.439	.455	.380	.308	.279	.256	.251
3.501	.939	.920	.885	.438	.454	.378	.305	.276	.254	.254
3.806	.940	.921	.886	.439	.454	.377	.304	.276	.253	.254
3.996	.939	.922	.886	.440	.453	.377	.303	.274	.252	.255
5.002	.938	.920	.884	.442	.451	.375	.301	.273	.251	.256
5.999	.939	.922	.885	.445	.450	.374	.300	.273	.249	.256
7.004	.939	.922	.885	.449	.450	.374	.300	.273	.245	.253
7.795	.938	.922	.884	.445	.450	.374	.299	.272	.245	.254

NPR	$z/(h_t/2) = 0.524$					
	x/L					
	.105	.192	.296	.470	.714	.923
1.810	.457	.439	.450	.531	.515	.544
1.999	.439	.400	.405	.382	.505	.473
2.503	.379	.382	.380	.319	.252	.364
3.002	.380	.381	.380	.318	.252	.225
3.501	.371	.387	.380	.315	.251	.228
3.806	.369	.389	.381	.315	.252	.227
3.996	.366	.390	.380	.313	.251	.229
5.002	.363	.391	.379	.310	.249	.230
5.999	.363	.391	.379	.309	.249	.231
7.004	.364	.389	.380	.308	.248	.229
7.795	.364	.389	.380	.308	.247	.229

NPR	ϕ, deg		
	0	26.5	53
1.810	.392	.786	.826
1.999	.316	.784	.824
2.503	.151	.786	.821
3.002	.148	.786	.823
3.501	.145	.789	.821
3.806	.141	.789	.822
3.996	.143	.790	.822
5.002	.152	.789	.820
5.999	.144	.788	.821
7.004	.134	.786	.821
7.795	.147	.786	.821

Table 11. Static Pressure Ratios for Maximum 17° A/B Configuration

(a) Orifices located on nozzle centerline and divergent flap

NPR	$y/(w_t/2) = 0$ x/L											
	-.499	-.385	-.276	-.176	-.087	-.007	.104	.191	.295	.469	.712	.921
1.808	.941	.938	.939	.919	.868	.376	.404	.409	.414	.435	.473	.510
2.005	.943	.940	.940	.922	.867	.337	.336	.346	.354	.383	.423	.457
2.502	.943	.937	.939	.921	.866	.270	.278	.276	.279	.303	.295	.374
3.000	.944	.939	.939	.920	.868	.270	.276	.273	.275	.302	.294	.265
3.502	.944	.940	.939	.921	.868	.271	.274	.271	.274	.301	.293	.265
3.798	.944	.941	.941	.920	.868	.270	.273	.270	.273	.301	.293	.265
4.006	.941	.941	.939	.921	.868	.271	.271	.269	.273	.301	.293	.263
5.001	.941	.941	.939	.920	.868	.266	.269	.267	.272	.301	.292	.263
5.998	.942	.942	.940	.921	.869	.265	.269	.267	.272	.300	.290	.263
7.002	.942	.943	.940	.921	.870	.266	.268	.266	.272	.300	.290	.262
7.317	.943	.943	.941	.921	.870	.267	.268	.267	.272	.300	.290	.262

NPR	x/L = 0.104 $y/(w_t/2)$				x/L = 0.191 $y/(w_t/2)$				x/L = 0.295 $y/(w_t/2)$			
	.000	.262	.525	.803	.000	.262	.525	.803	.000	.262	.525	.803
1.808	.404	.358	.299	.562	.409	.370	.381	.512	.414	.392	.471	.483
2.005	.336	.289	.251	.546	.346	.290	.384	.486	.354	.321	.468	.436
2.502	.278	.218	.215	.519	.276	.226	.441	.459	.279	.252	.451	.409
3.000	.276	.219	.217	.520	.273	.226	.436	.459	.275	.252	.449	.408
3.502	.274	.218	.217	.520	.271	.227	.442	.459	.274	.251	.448	.408
3.798	.273	.217	.217	.519	.270	.226	.445	.460	.273	.251	.448	.408
4.006	.271	.217	.218	.520	.269	.228	.434	.460	.273	.252	.447	.408
5.001	.269	.217	.218	.520	.267	.227	.438	.459	.272	.250	.446	.408
5.998	.269	.216	.218	.521	.267	.227	.439	.459	.272	.250	.446	.407
7.002	.268	.217	.222	.522	.266	.229	.427	.460	.272	.250	.446	.407
7.317	.268	.213	.219	.521	.267	.227	.438	.459	.272	.251	.447	.407

NPR	x/L = 0.469 $y/(w_t/2)$				x/L = 0.712 $y/(w_t/2)$				x/L = 0.921 $y/(w_t/2)$			
	.000	.262	.525	.803	.000	.262	.525	.803	.000	.262	.525	.803
1.808	.435	.425	.463	.458	.473	.476	.495	.503	.510	.516	.535	.540
2.005	.383	.368	.403	.388	.423	.428	.415	.393	.457	.464	.484	.498
2.502	.303	.297	.336	.344	.295	.265	.255	.269	.324	.295	.354	.352
3.000	.302	.293	.335	.342	.294	.267	.254	.269	.265	.241	.224	.211
3.502	.301	.293	.333	.341	.293	.267	.254	.269	.265	.240	.225	.212
3.798	.301	.294	.331	.341	.293	.267	.253	.269	.265	.240	.225	.212
4.006	.301	.292	.331	.341	.293	.266	.253	.269	.263	.239	.225	.211
5.001	.301	.290	.329	.340	.292	.266	.252	.270	.263	.238	.225	.211
5.998	.300	.289	.328	.339	.290	.265	.251	.270	.263	.238	.225	.211
7.002	.300	.286	.328	.338	.290	.265	.249	.268	.262	.237	.223	.209
7.317	.300	.289	.328	.338	.290	.265	.249	.269	.262	.237	.223	.209

Table 11. Concluded

(b) Orifices located on nozzle sidewall and convergent flap lip

NPR	z/(h_t/2) = 0 x/L									
	-.453	-.352	-.255	-.077	.105	.192	.296	.470	.714	.923
1.808	.929	.908	.875	.452	.525	.486	.447	.437	.501	.540
2.005	.928	.912	.877	.444	.490	.440	.418	.368	.390	.513
2.502	.928	.909	.875	.435	.479	.413	.372	.326	.273	.340
3.000	.927	.913	.876	.433	.479	.411	.371	.325	.272	.229
3.502	.929	.914	.878	.433	.479	.411	.372	.327	.271	.227
3.798	.928	.913	.878	.432	.478	.410	.372	.327	.271	.226
4.006	.928	.914	.878	.432	.478	.410	.371	.326	.271	.226
5.001	.928	.914	.878	.433	.478	.409	.371	.328	.269	.224
5.998	.928	.916	.878	.437	.477	.408	.370	.327	.269	.223
7.002	.929	.916	.879	.445	.477	.407	.367	.325	.271	.226
7.317	.929	.916	.879	.448	.476	.407	.366	.324	.271	.227

NPR	z/(h_t/2) = 0.524 x/L					
	.105	.192	.296	.470	.714	.923
1.808	.529	.496	.465	.444	.498	.541
2.005	.496	.478	.432	.379	.368	.511
2.502	.456	.449	.400	.339	.264	.354
3.000	.457	.449	.401	.338	.263	.225
3.502	.457	.450	.402	.339	.263	.224
3.798	.457	.450	.403	.339	.263	.224
4.006	.457	.449	.402	.339	.262	.224
5.001	.457	.449	.403	.340	.262	.222
5.998	.458	.449	.402	.339	.261	.222
7.002	.459	.449	.403	.338	.260	.223
7.317	.458	.448	.402	.338	.261	.224

NPR	ϕ, deg		
	0	26.5	53
1.808	.396	.764	.839
2.005	.337	.762	.840
2.502	.270	.763	.838
3.000	.270	.764	.841
3.502	.271	.767	.840
3.798	.270	.767	.840
4.006	.271	.768	.841
5.001	.266	.769	.840
5.998	.265	.769	.840
7.002	.266	.772	.841
7.317	.267	.772	.841

Table 12. Static Pressure Ratios for Maximum 0° A/B Configuration

(a) Orifices located on nozzle centerline and divergent flap

NPR	$y/(w_t/2) = 0$											
	x/L											
	-.499	-.385	-.276	-.176	-.087	-.007	.104	.191	.295	.469	.712	.921
1.809	.935	.934	.929	.908	.853	.221	.238	.289	.337	.364	.409	.542
2.004	.934	.931	.930	.910	.853	.220	.236	.290	.337	.364	.303	.468
2.500	.935	.932	.932	.910	.851	.217	.226	.287	.336	.364	.300	.272
3.002	.935	.936	.932	.909	.853	.210	.218	.285	.340	.363	.298	.237
3.505	.936	.936	.932	.909	.852	.202	.212	.285	.344	.363	.297	.236
3.804	.936	.937	.932	.909	.853	.197	.210	.286	.345	.363	.296	.235
3.999	.935	.937	.932	.900	.853	.195	.208	.287	.347	.364	.296	.235
5.004	.935	.936	.932	.908	.852	.179	.204	.290	.349	.364	.295	.233
6.005	.936	.938	.934	.910	.853	.139	.203	.292	.350	.364	.294	.230
6.995	.937	.938	.934	.909	.853	.173	.204	.292	.351	.364	.294	.230

NPR	x/L = 0.104				x/L = 0.191				x/L = 0.295			
	$y/(w_t/2)$				$y/(w_t/2)$				$y/(w_t/2)$			
	.000	.262	.525	.803	.000	.262	.525	.803	.000	.262	.525	.803
1.809	.238	.227	.401	.400	.289	.304	.391	.423	.337	.396	.391	.392
2.004	.236	.227	.399	.396	.290	.309	.388	.422	.337	.395	.391	.389
2.500	.226	.227	.396	.394	.287	.317	.386	.418	.336	.394	.389	.385
3.002	.218	.230	.393	.394	.285	.320	.384	.417	.340	.394	.386	.382
3.505	.212	.230	.390	.394	.285	.321	.382	.416	.344	.396	.383	.380
3.804	.210	.230	.390	.396	.286	.321	.382	.415	.345	.397	.383	.379
3.999	.208	.231	.389	.396	.287	.322	.382	.415	.347	.397	.382	.379
5.004	.204	.234	.386	.398	.290	.324	.381	.414	.349	.396	.382	.378
6.005	.203	.232	.386	.401	.292	.323	.382	.413	.350	.395	.382	.377
6.995	.204	.238	.387	.402	.292	.325	.383	.413	.351	.390	.381	.377

NPR	x/L = 0.469				x/L = 0.712				x/L = 0.921			
	$y/(w_t/2)$				$y/(w_t/2)$				$y/(w_t/2)$			
	.000	.262	.525	.803	.000	.262	.525	.803	.000	.262	.525	.803
1.809	.364	.365	.346	.348	.409	.409	.445	.454	.542	.543	.541	.533
2.004	.364	.362	.344	.344	.303	.290	.279	.332	.468	.467	.469	.477
2.500	.364	.361	.343	.341	.300	.291	.277	.271	.272	.241	.298	.322
3.002	.363	.362	.343	.339	.298	.290	.275	.272	.237	.235	.237	.235
3.505	.363	.362	.343	.337	.297	.289	.274	.272	.236	.234	.236	.234
3.804	.363	.362	.343	.337	.296	.289	.274	.273	.235	.233	.235	.233
3.999	.364	.363	.343	.336	.296	.289	.274	.274	.235	.232	.235	.234
5.004	.364	.362	.342	.336	.295	.298	.272	.274	.233	.231	.233	.232
6.005	.364	.362	.341	.335	.294	.288	.272	.275	.230	.227	.230	.230
6.995	.364	.362	.342	.334	.294	.288	.271	.275	.230	.226	.229	.230

Table 12. Concluded

(b) Orifices located on nozzle sidewall and convergent flap lip

NPR	$z/(h_t/2) = 0$									
	x/L									
	-.453	-.352	-.255	-.077	.105	.192	.296	.470	.714	.923
1.809	.924	.907	.875	.501	.533	.461	.370	.312	.465	.520
2.004	.024	.906	.876	.498	.531	.460	.370	.311	.347	.471
2.500	.925	.905	.874	.495	.530	.458	.368	.311	.259	.278
3.002	.925	.908	.876	.494	.531	.458	.367	.311	.256	.262
3.505	.924	.909	.877	.493	.531	.458	.366	.309	.253	.264
3.804	.925	.910	.876	.493	.531	.458	.366	.309	.252	.264
3.999	.924	.910	.876	.493	.531	.458	.366	.308	.252	.264
5.004	.924	.909	.876	.492	.531	.457	.365	.306	.252	.264
6.005	.926	.912	.878	.491	.531	.457	.364	.303	.252	.264
6.995	.926	.911	.878	.490	.531	.457	.363	.302	.251	.265

NPR	$z/(h_t/2) = 0.524$					
	x/L					
	.105	.192	.296	.470	.714	.923
1.809	.484	.420	.397	.329	.473	.521
2.004	.481	.421	.396	.328	.328	.474
2.500	.481	.419	.394	.326	.268	.268
3.002	.482	.418	.394	.323	.270	.242
3.505	.482	.418	.394	.321	.269	.242
3.804	.483	.417	.395	.321	.268	.242
3.999	.483	.418	.395	.321	.268	.242
5.004	.483	.417	.394	.321	.266	.242
6.005	.484	.418	.393	.320	.263	.242
6.995	.485	.418	.393	.320	.262	.243

NPR	φ, deg		
	0	26.5	45
1.809	.221	.737	.828
2.004	.220	.737	.828
2.500	.217	.736	.827
3.002	.210	.735	.828
3.505	.202	.737	.828
3.804	.197	.737	.827
3.999	.195	.737	.828
5.004	.179	.736	.826
6.005	.139	.735	.827
6.995	.123	.736	.827

Figure 1. Hardware for simulated single-engine propulsion system for high-pressure air. All dimensions are given in inches unless otherwise noted.
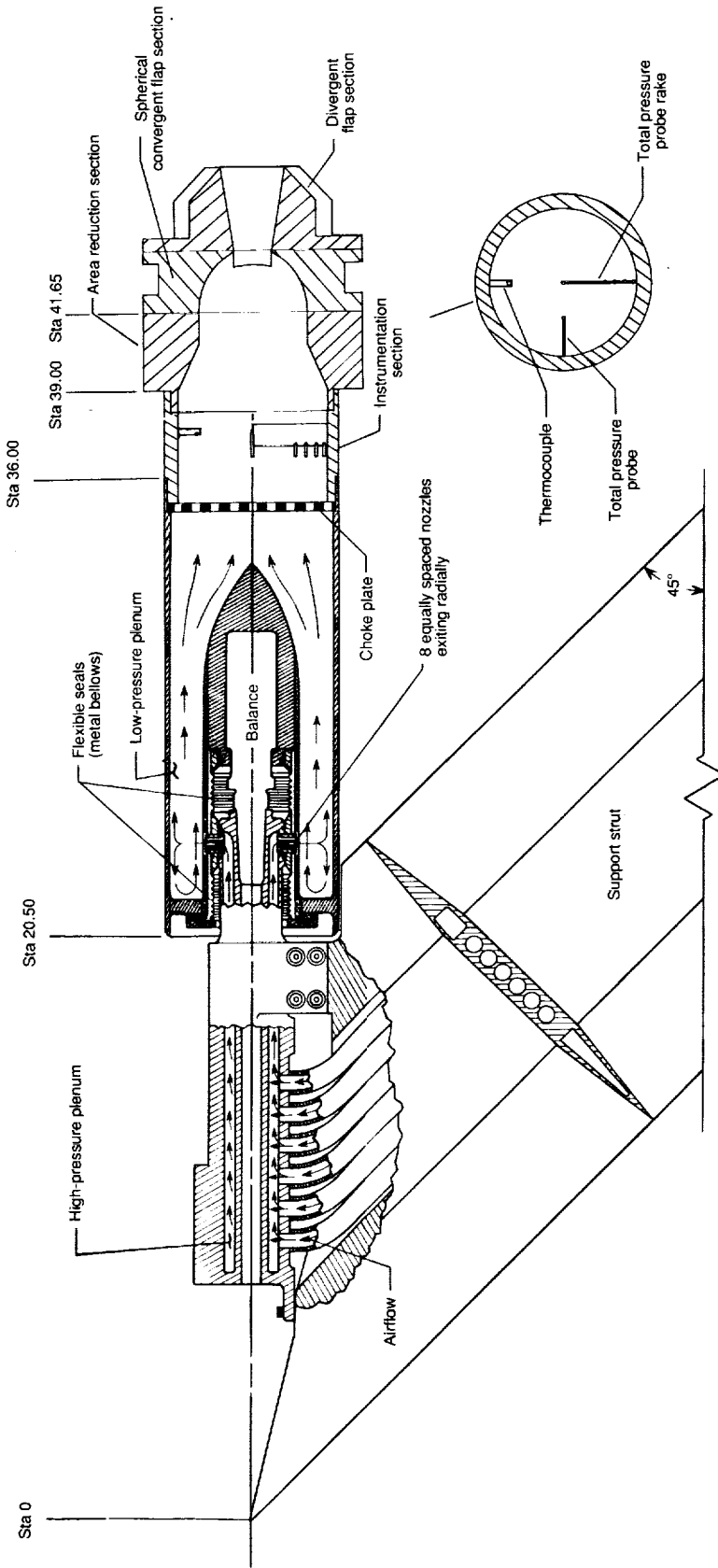
(a) Sketch showing side view.

Sta 0

Sta 20.50

Sta 36.00

Sta 39.00   Sta 41.65

Area reduction section

Spherical convergent flap section

Divergent flap section

Instrumentation section

Choke plate

8 equally spaced nozzles exiting radially

Balance

Low-pressure plenum

Flexible seals (metal bellows)

High-pressure plenum

Airflow

Total pressure probe rake

Thermocouple

Total pressure probe

Support strut

45°

L-90-58

(b) Photograph.

Figure 1. Continued.

Mounted on balance (metric)

Mounted on support system (nonmetric)

Low-pressure plenum

Balance

Bellows

8 multiholed sonic nozzles

High-pressure flow

Balance cable
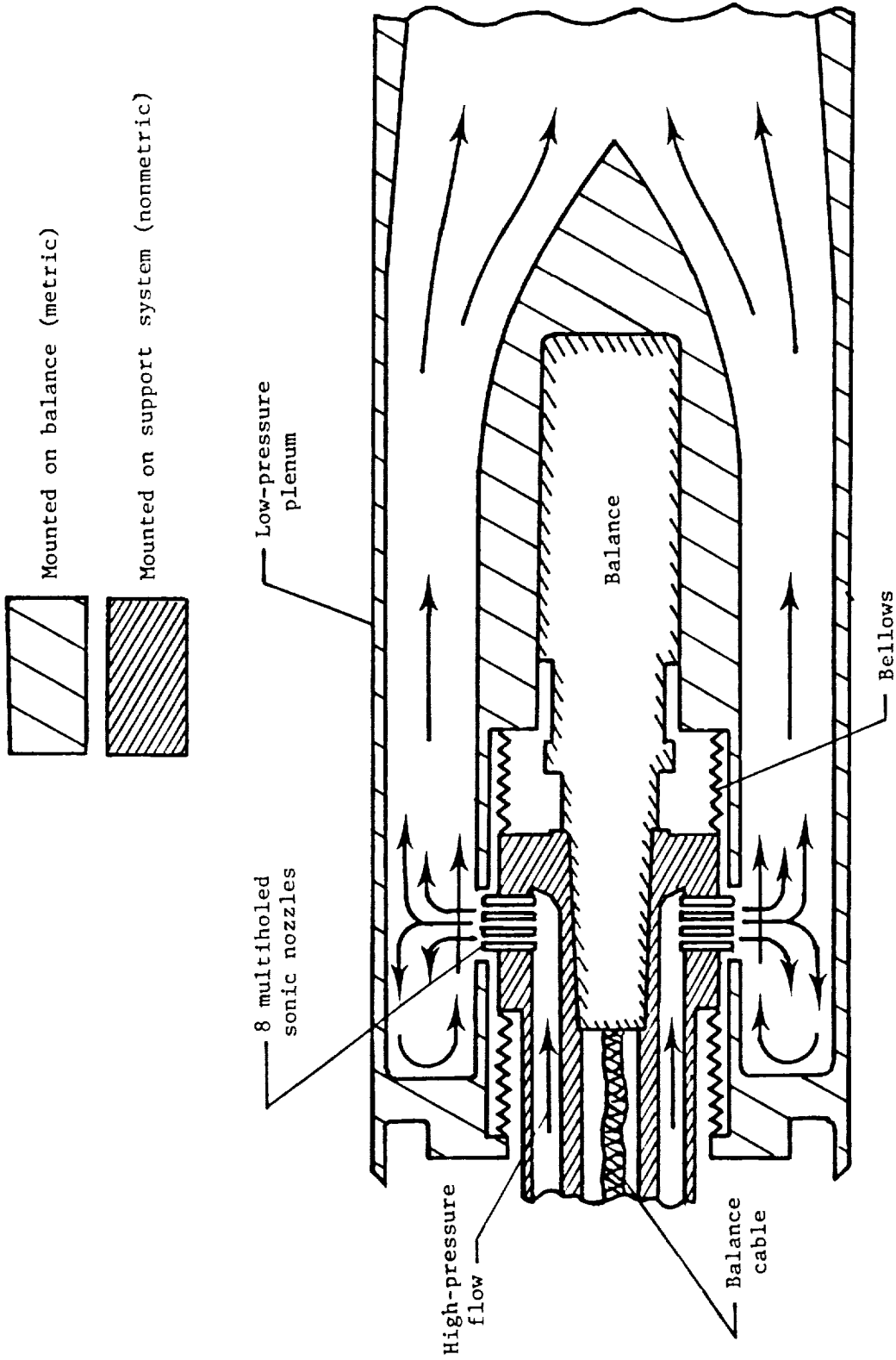
(c) Schematic cross section of flow transfer system.

Figure 1. Concluded.

Sta 39.00   Sta 41.65

A

5.064   3.820

1.60

2.65

A
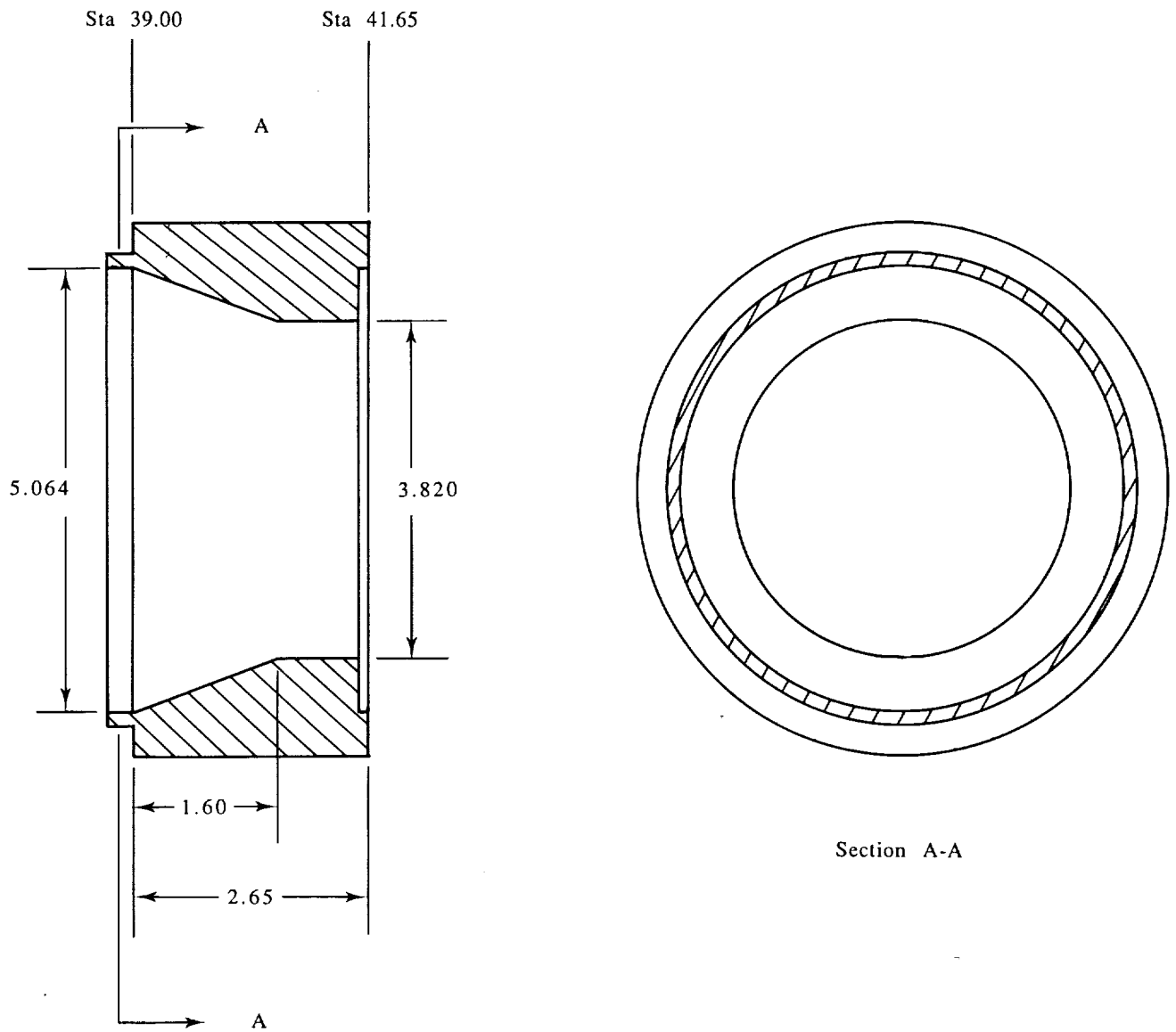
Figure 2. Area reduction section. All dimensions are given in inches.

Section A-A
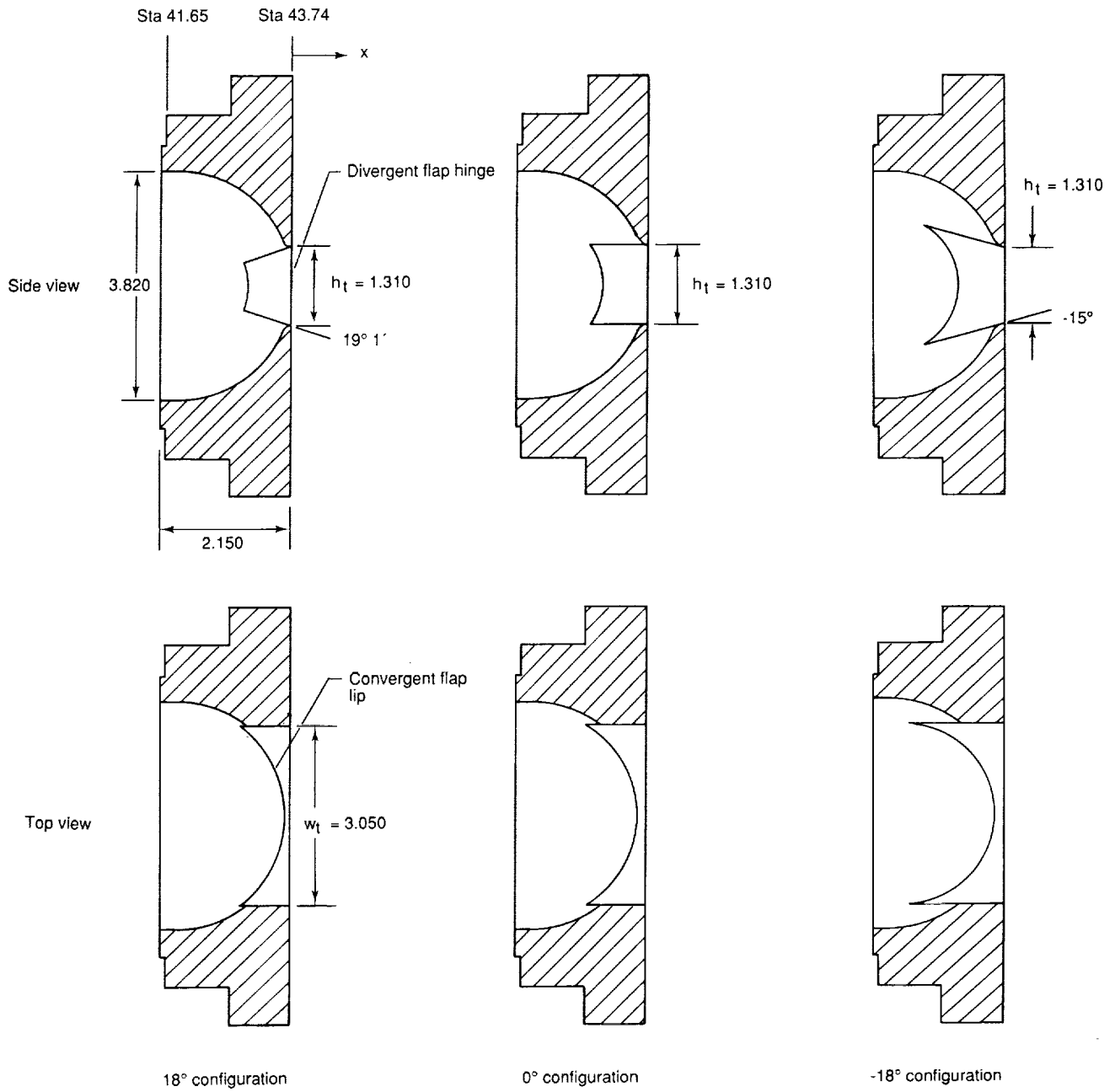
(a) Dry power.

Figure 3. Geometry of nozzle spherical convergent flap. All views are for planar cuts through the model centerline. Dimensions are given in inches unless noted otherwise.

Sta 41.65   Sta 43.56

Side view

Divergent flap
hinge

3.820

$h_t = 2.468$

35° 35′

$h_t = 2.374$

-18°

$h_t = 2.290$

1.85

Top view

Convergent flap
lip

$w_t = 3.050$

35° configuration

17° configuration

0° configuration
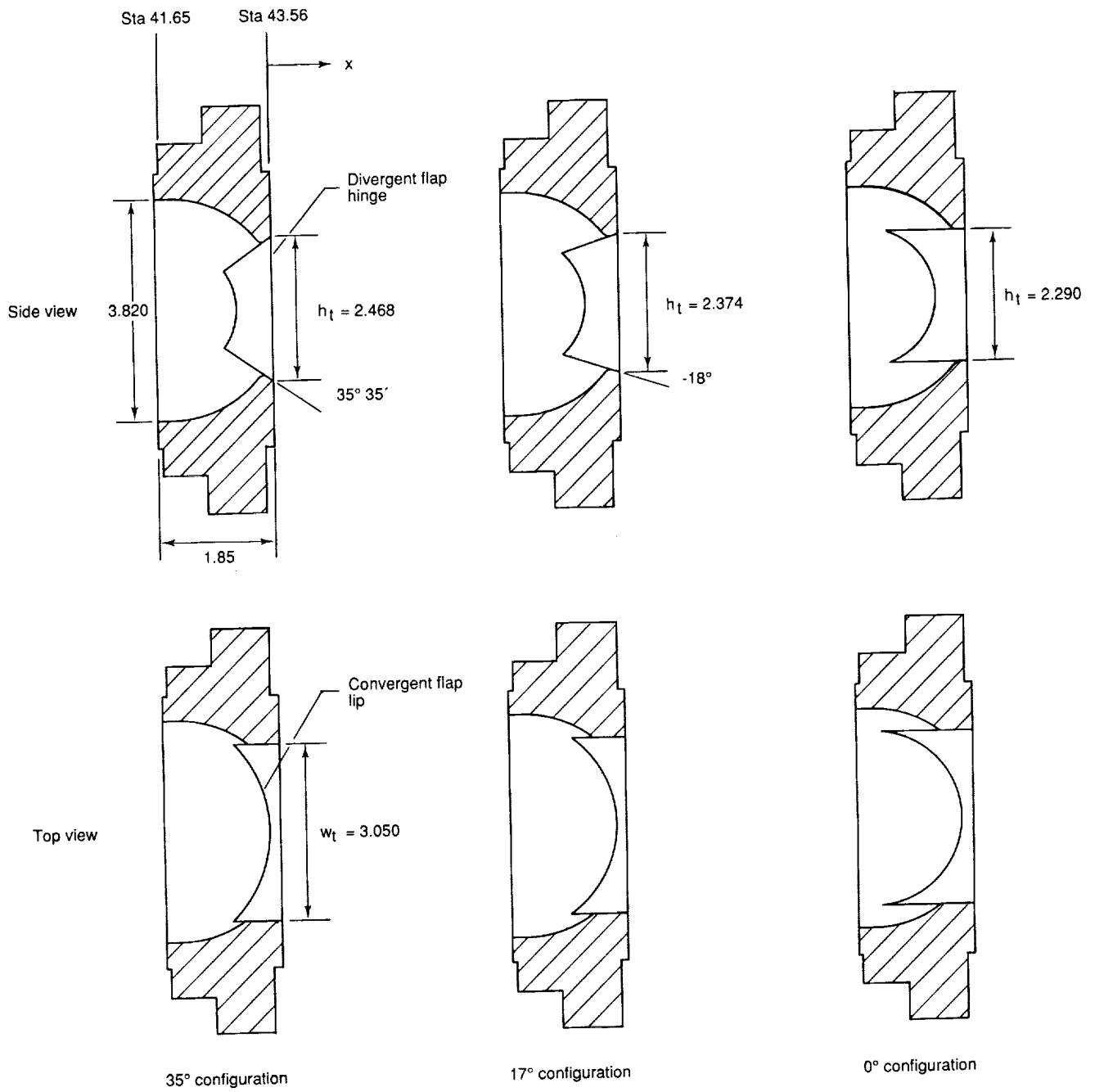
(b) Maximum A/B power.

Figure 3. Concluded.

Top view

5.064

x = 0

Dry power	A_t, in^2
18°	3.991
0°	4.013
-18°	4.057

L = 2.87

Side view

1.91

α

12.86°

4.58°

Subsonic cruise
divergent flap setting

Supersonic cruise
divergent flap setting

1.90

Sta 41.84   Sta 43.74   Sta 46.61

Rear view
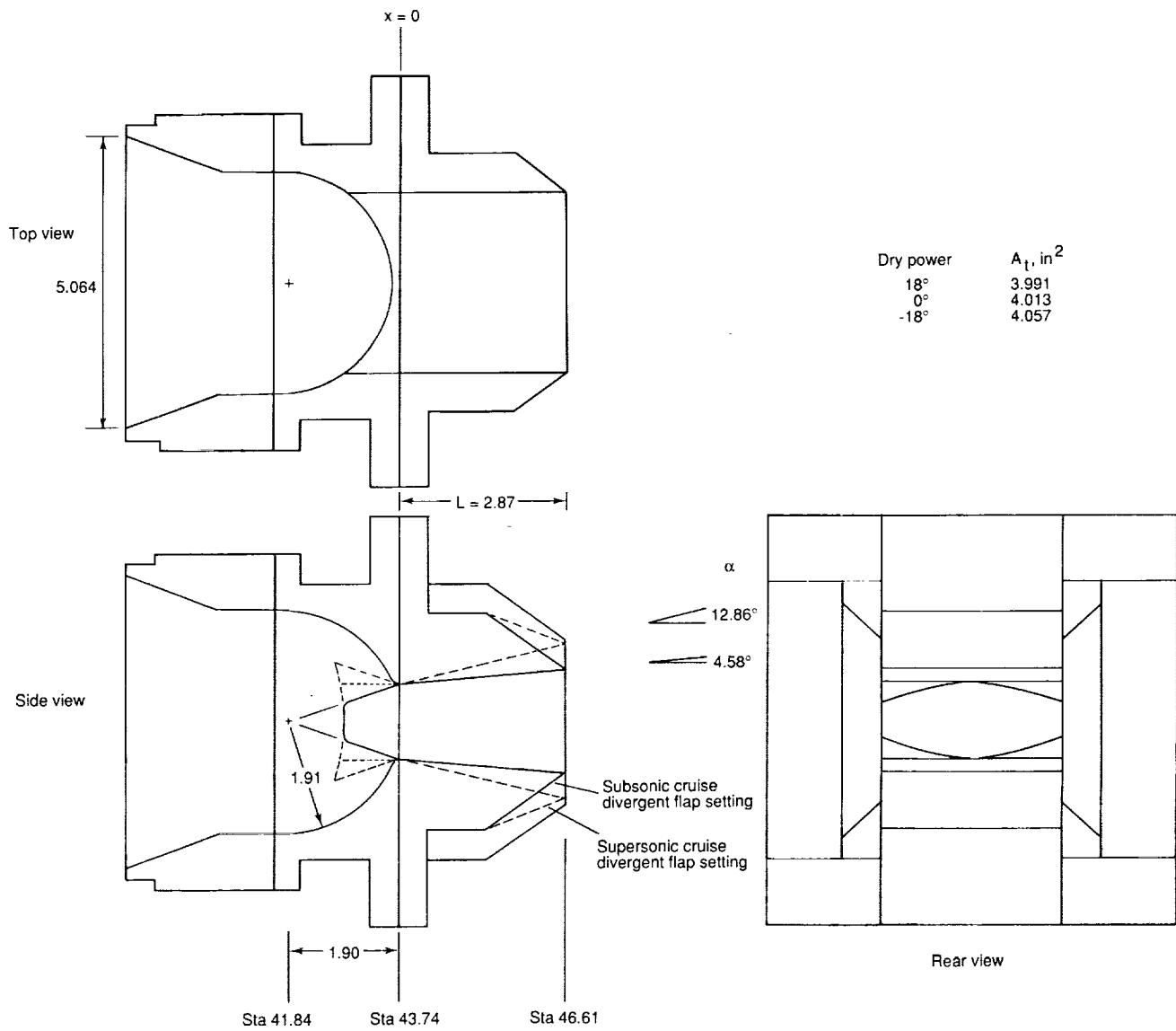
(a) Dry power.

Figure 4. Schematic of nozzle geometry. All dimensions are given in inches unless otherwise noted.

x = 0

Top view

5.064

+

Maximum A/B	A_t, in^2
35°	6.940
17°	6.990
0°	6.983

L = 2.87

α
4.58°

Side view

+

1.91

Rear view

1.60

Sta 41.84   Sta 43.56   Sta 46.43
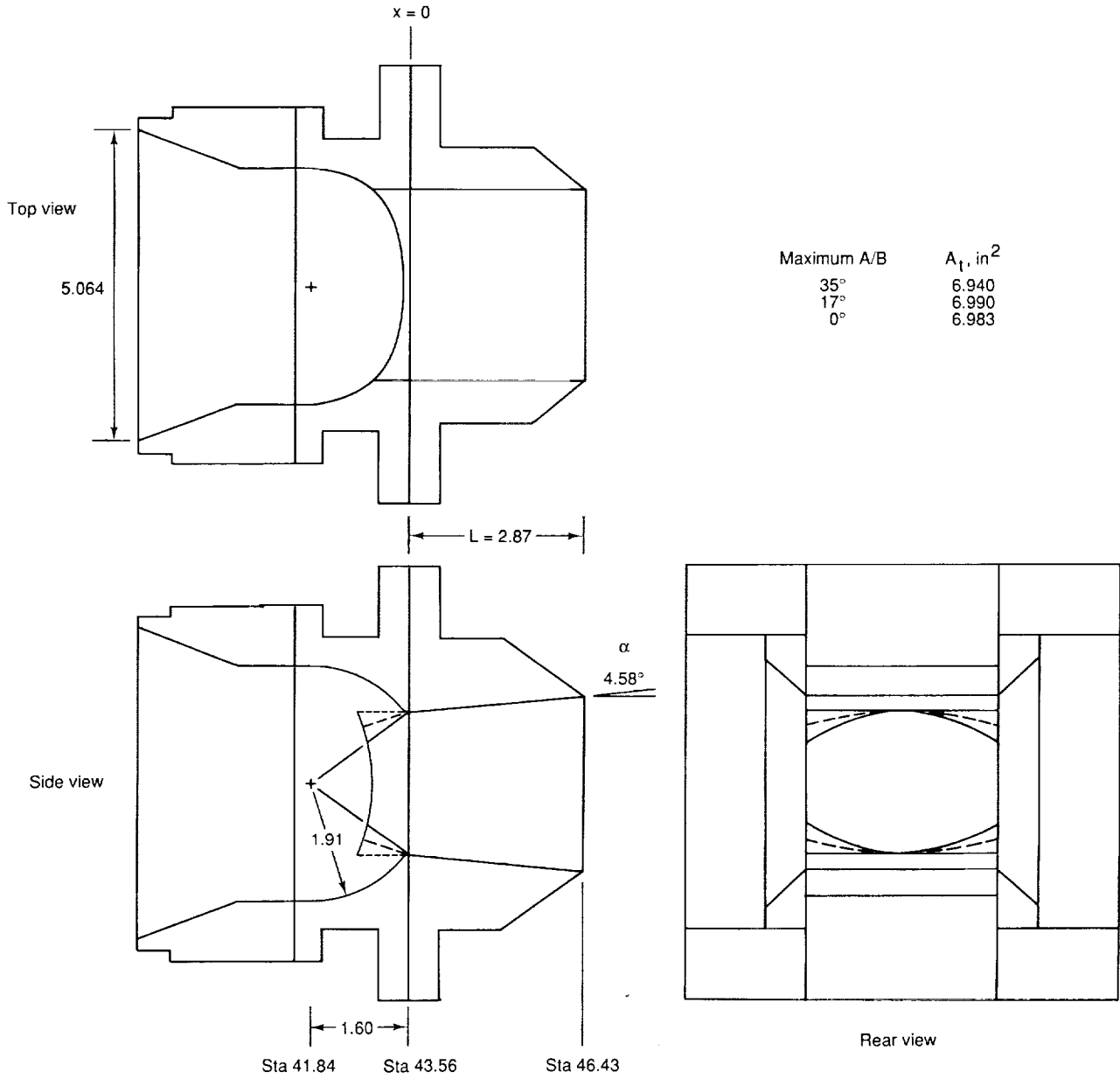
(b) Maximum A/B power.

Figure 4. Concluded.

37
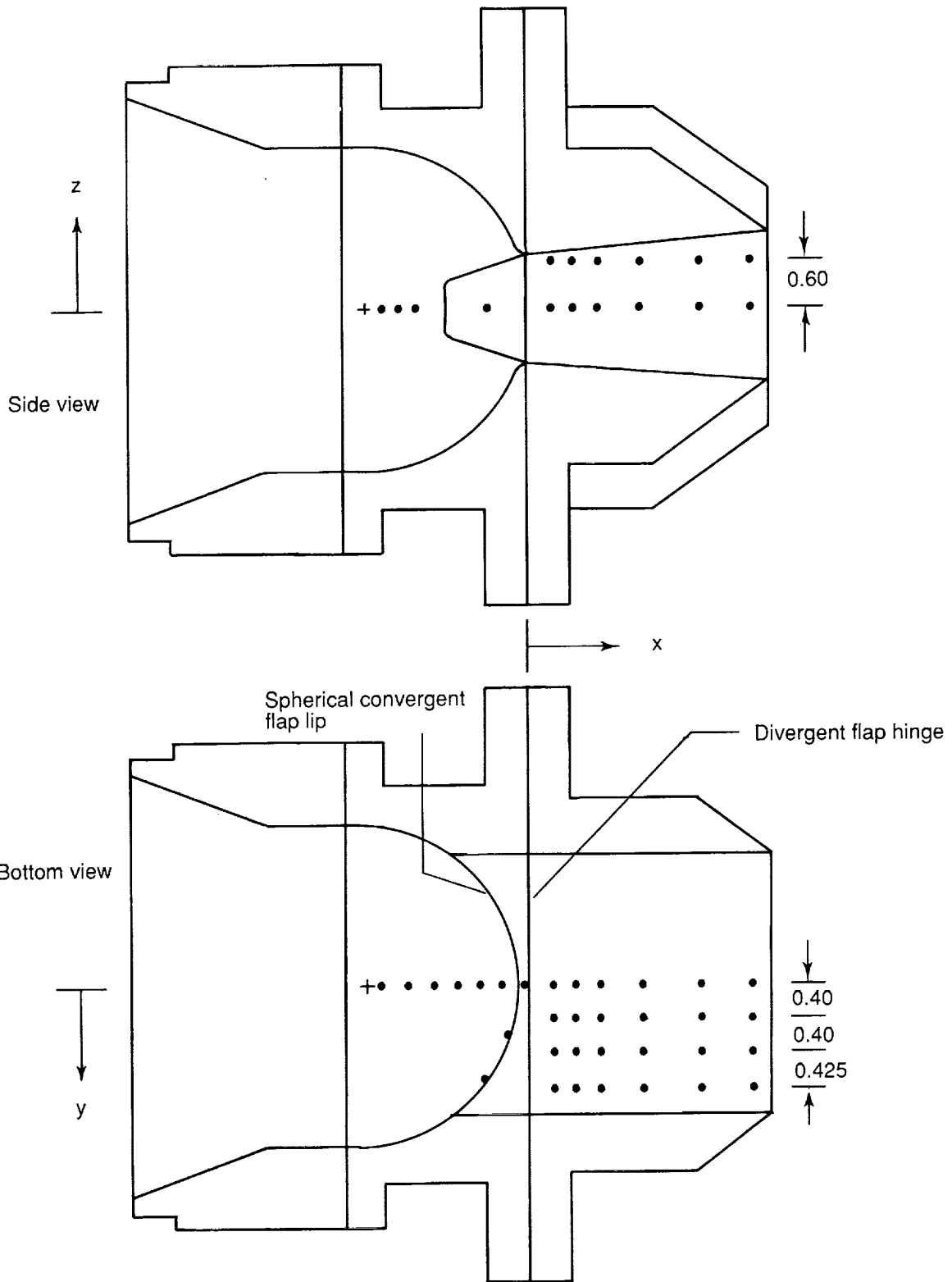
(a) Nozzle centerline, divergent flap, and sidewall orifices.

Figure 5. Locations of nozzle internal static pressure orifices. Dimensions are given in inches unless noted otherwise.
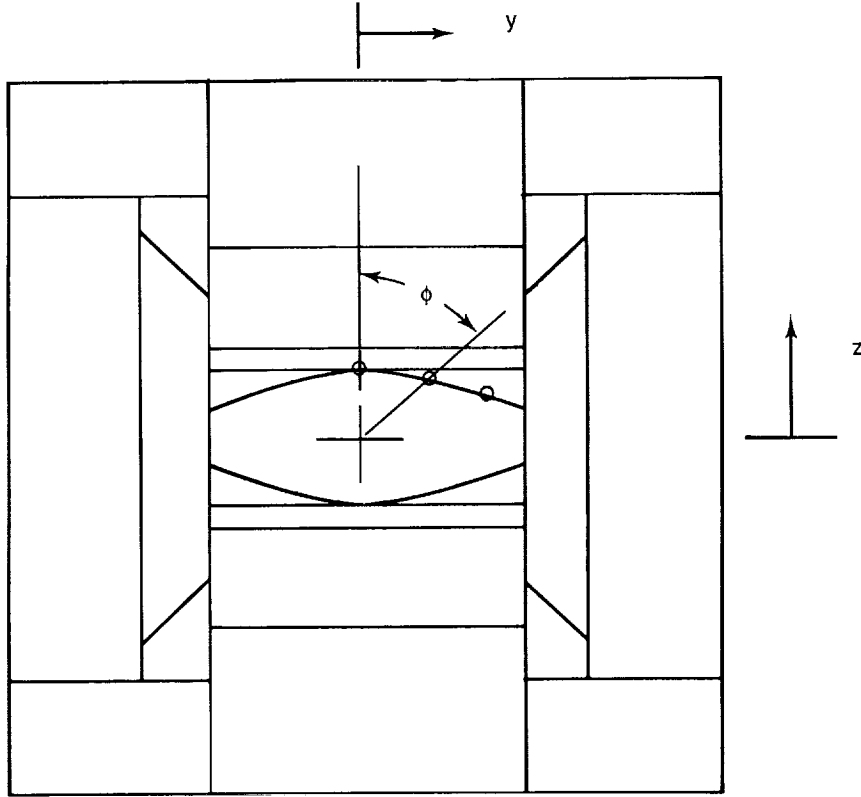
Dry power configurations				
Configuration	ϕ, deg	x/L	$y/(w_t/2)$	$z/(h_t/2)$
18°	0	-0.007	0.000	0.991
	33	-.070	.313	1.121
	66	-.221	.875	.889
0°	0	-0.007	0.000	1.000
	33	-.074	.320	1.148
	60	-.252	.854	1.148
-18°	0	-0.007	0.000	1.000
	33	-.082	.334	1.195
	53	-.282	.821	1.440

A/B power configurations				
Configuration	ϕ, deg	x/L	$y/(w_t/2)$	$z/(h_t/2)$
35°	0	-0.007	0.000	0.990
	26.5	-.071	.379	1.021
	53	-.191	.835	.838
17°	0	-0.007	0.000	0.995
	26.5	-.078	.388	1.037
	53	-.259	.894	.897
0°	0	-0.007	0.000	1.000
	26.5	-.090	.397	1.061
	45	-.267	.797	1.061

(b) Convergent flap lip orifices.

Figure 5. Concluded.
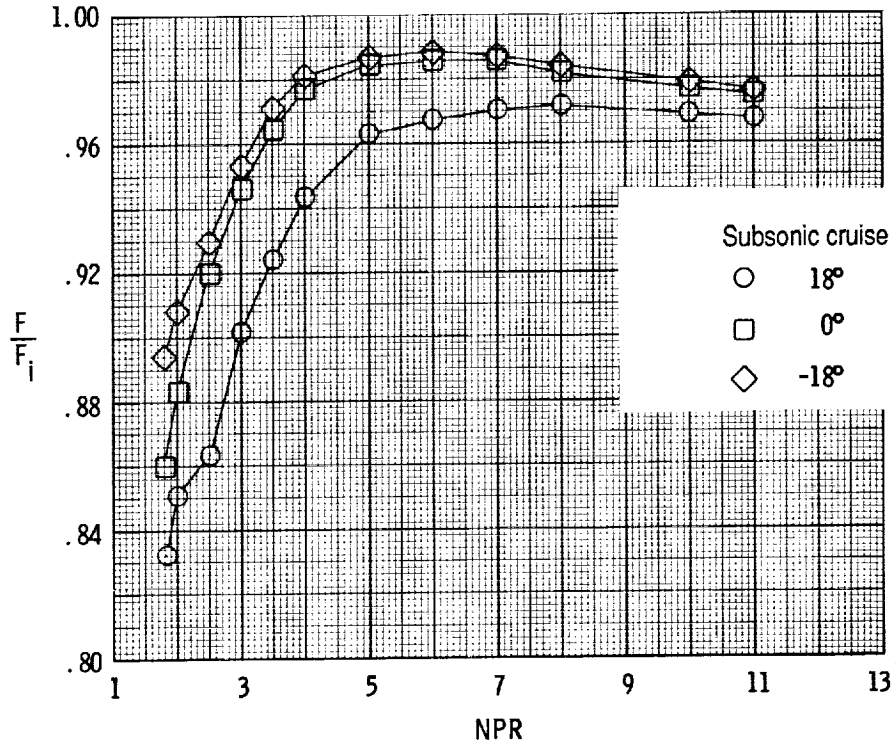
(a) Internal thrust ratio curves.
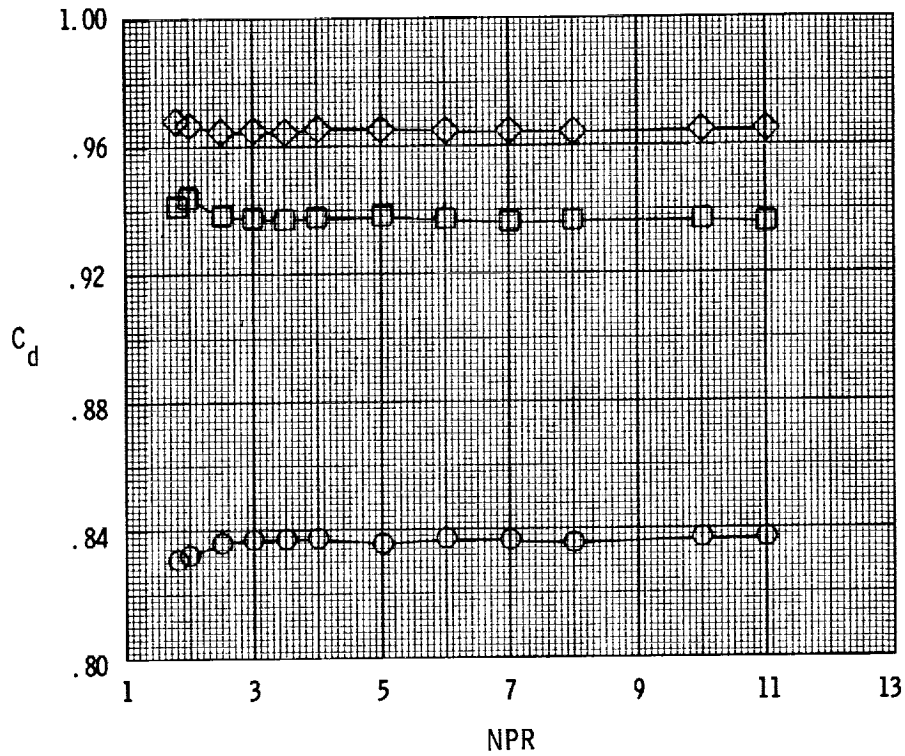
(b) Discharge coefficient curves.

Figure 6. Nozzle internal performance for dry power subsonic cruise configurations.

40
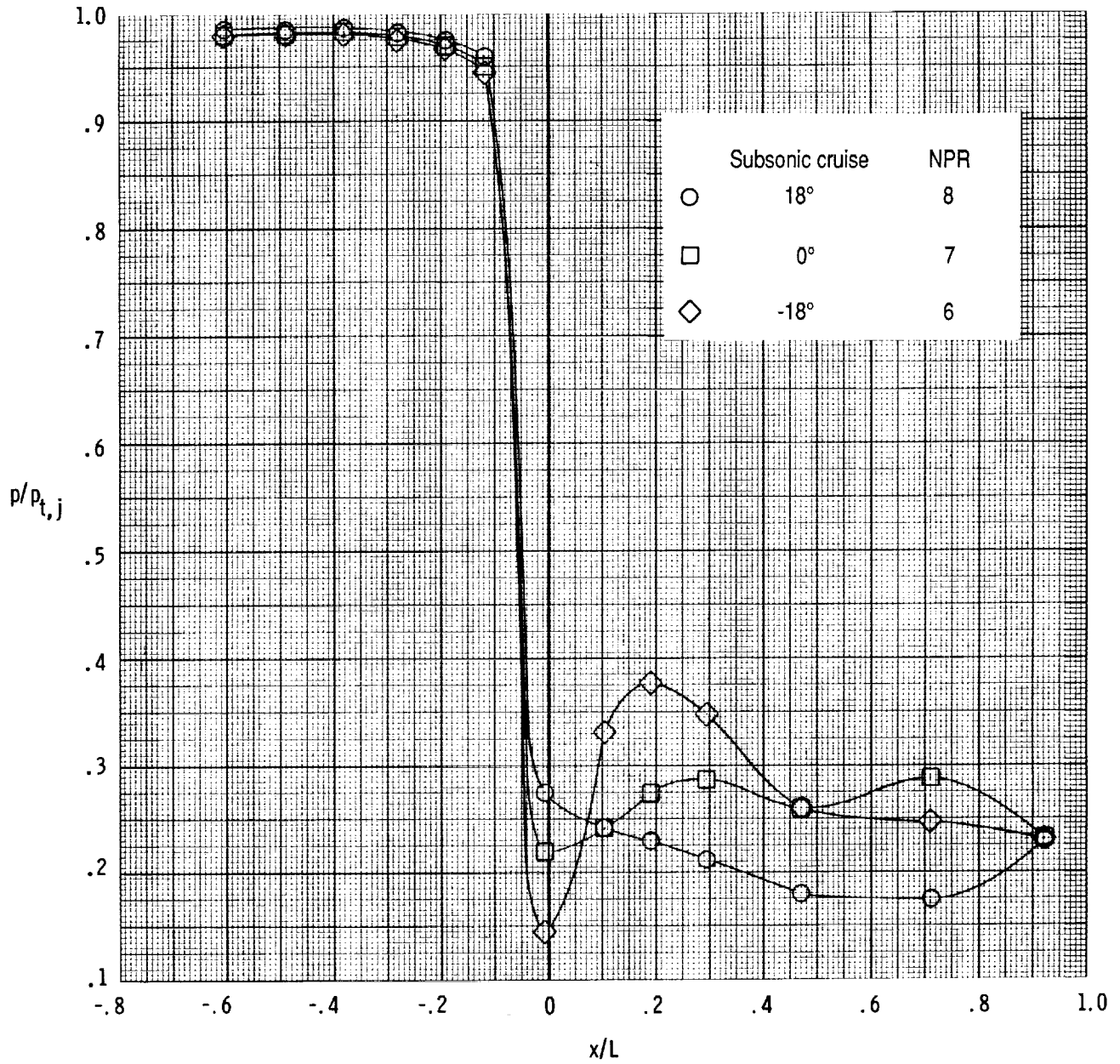
(a) Centerline distributions of convergent and divergent flaps.

Figure 7. Static pressure distributions for dry power subsonic cruise configurations at a NPR near peak performance.
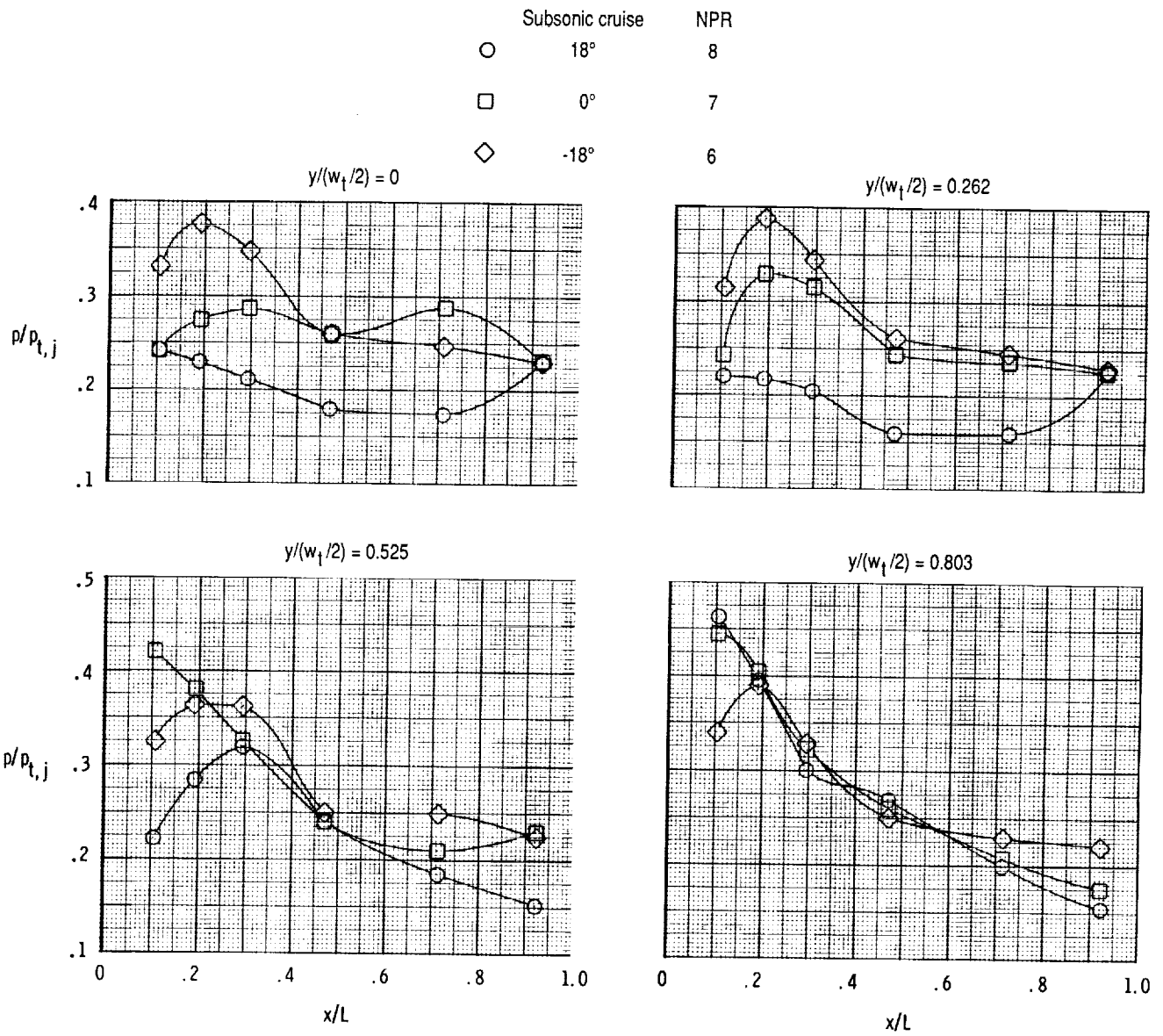
(b) Divergent flap distributions at different spanwise locations.
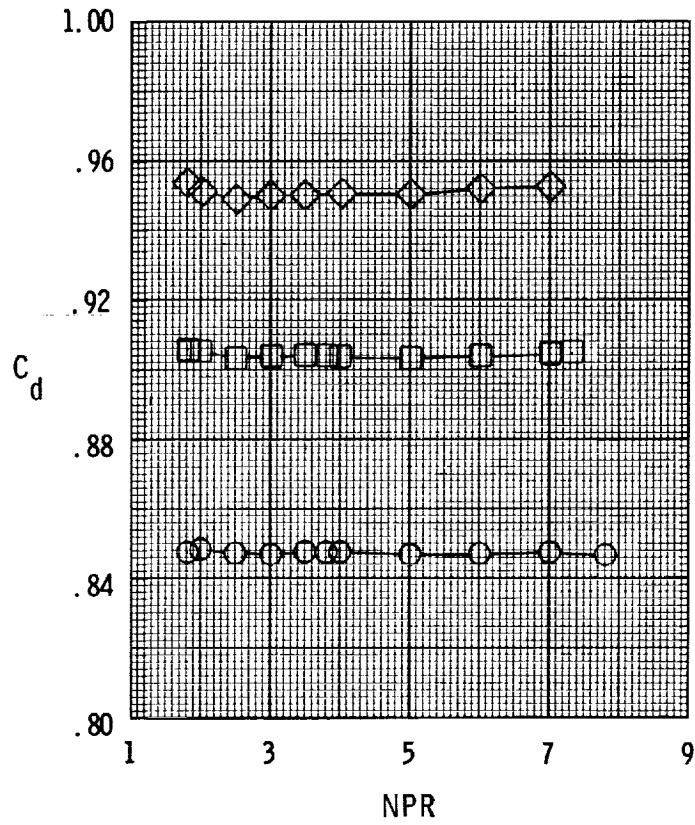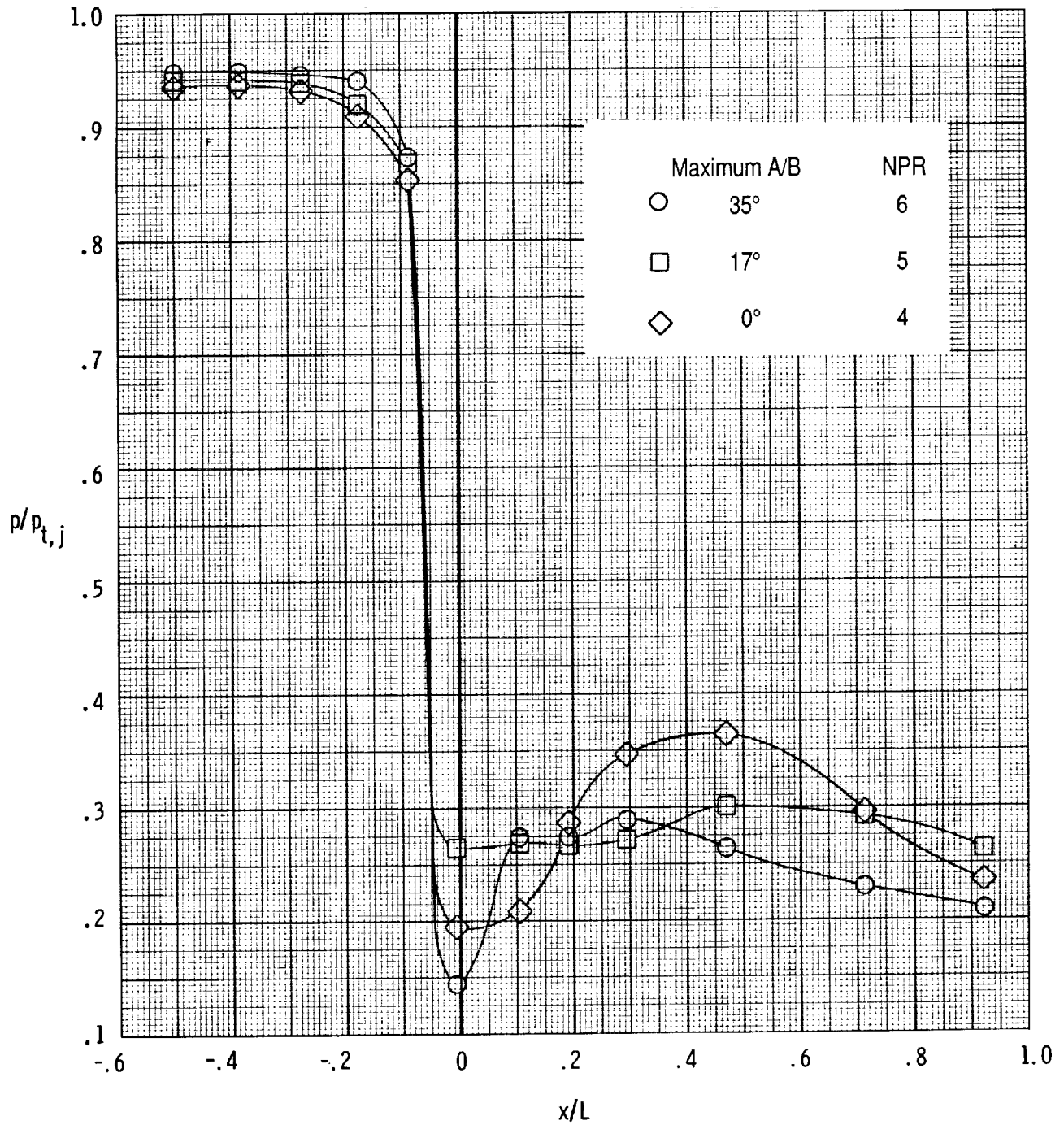
Figure 7. Continued.
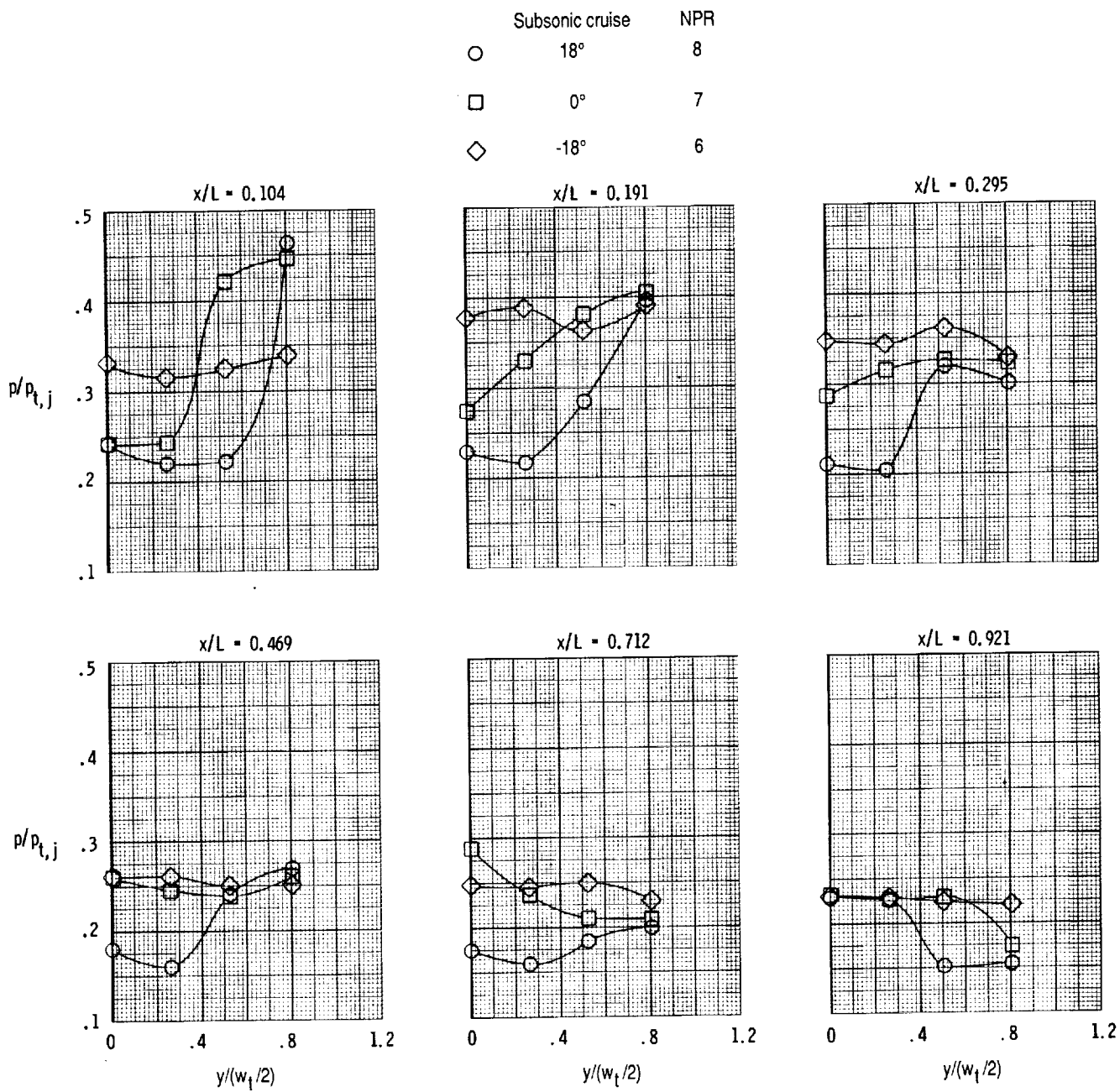
(c) Divergent flap lateral distributions.

Figure 7. Continued.
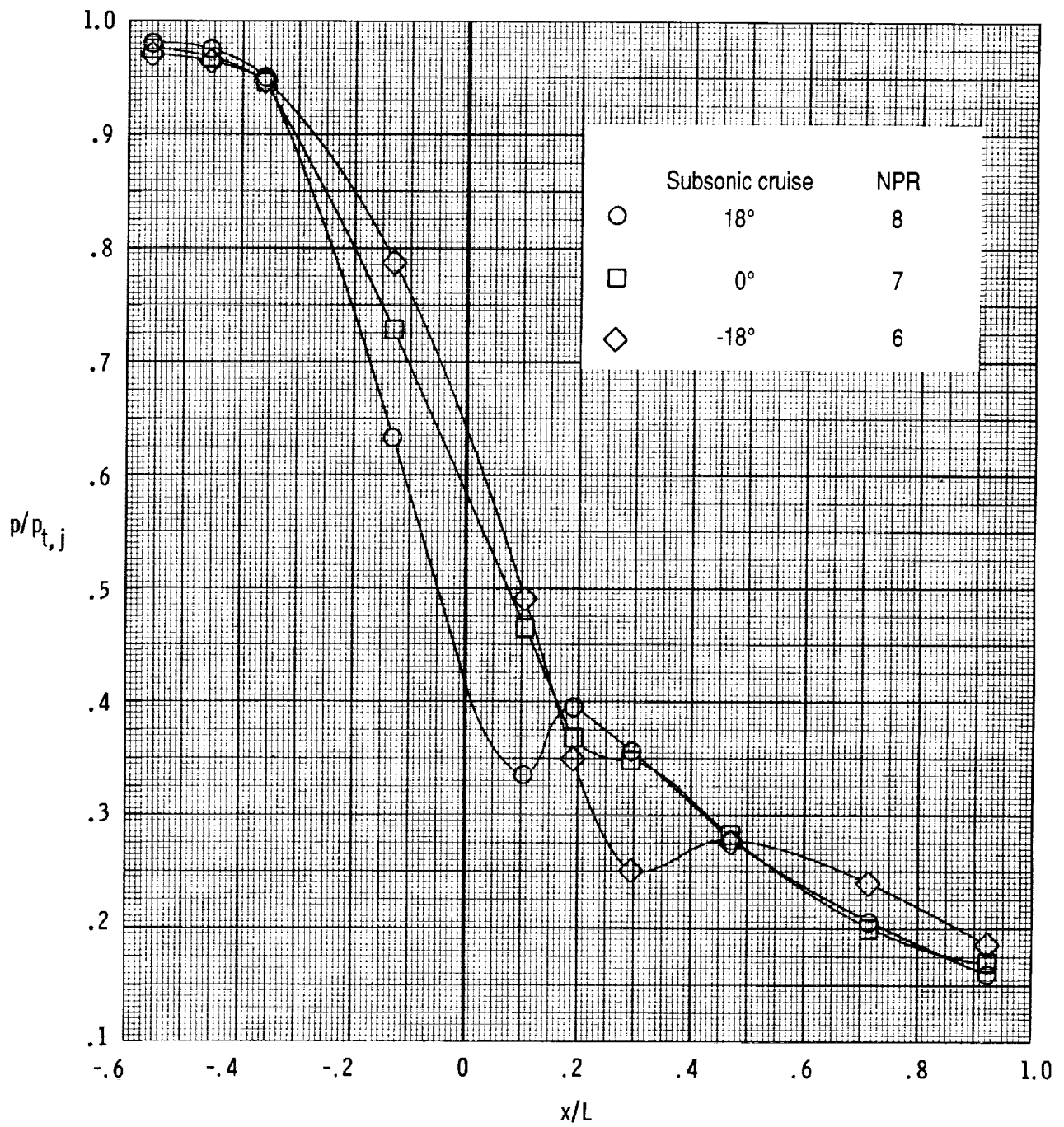
(d) Sidewall centerline distributions.

Figure 7. Concluded.
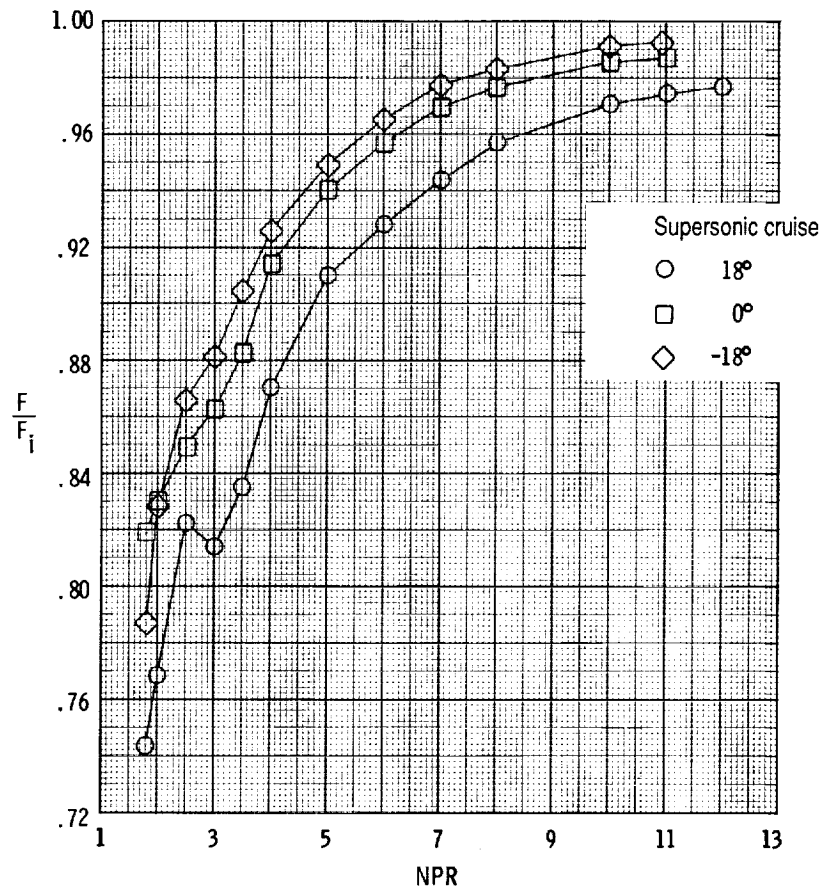
(a) Internal thrust ratio curves.
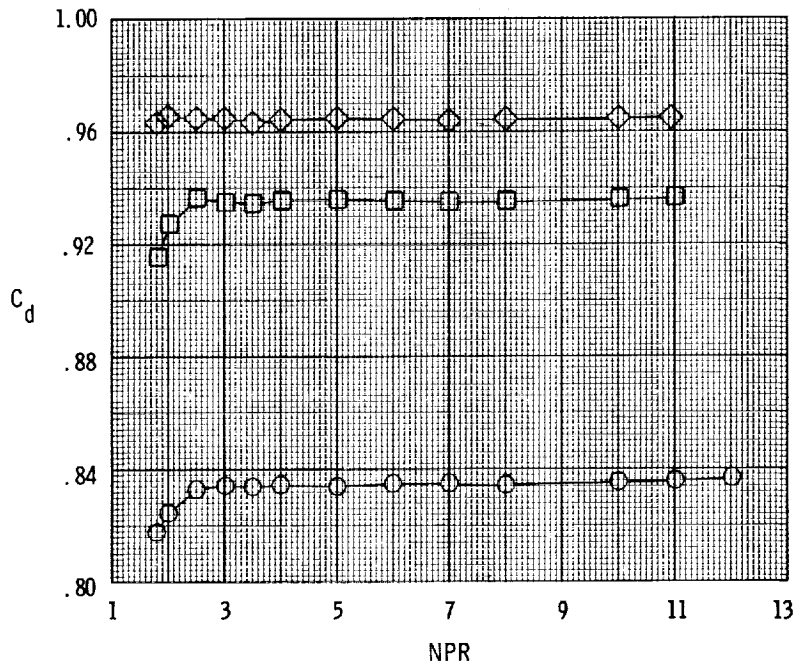
(b) Discharge coefficient curves.

Figure 8. Nozzle internal performance for dry power supersonic cruise configurations.
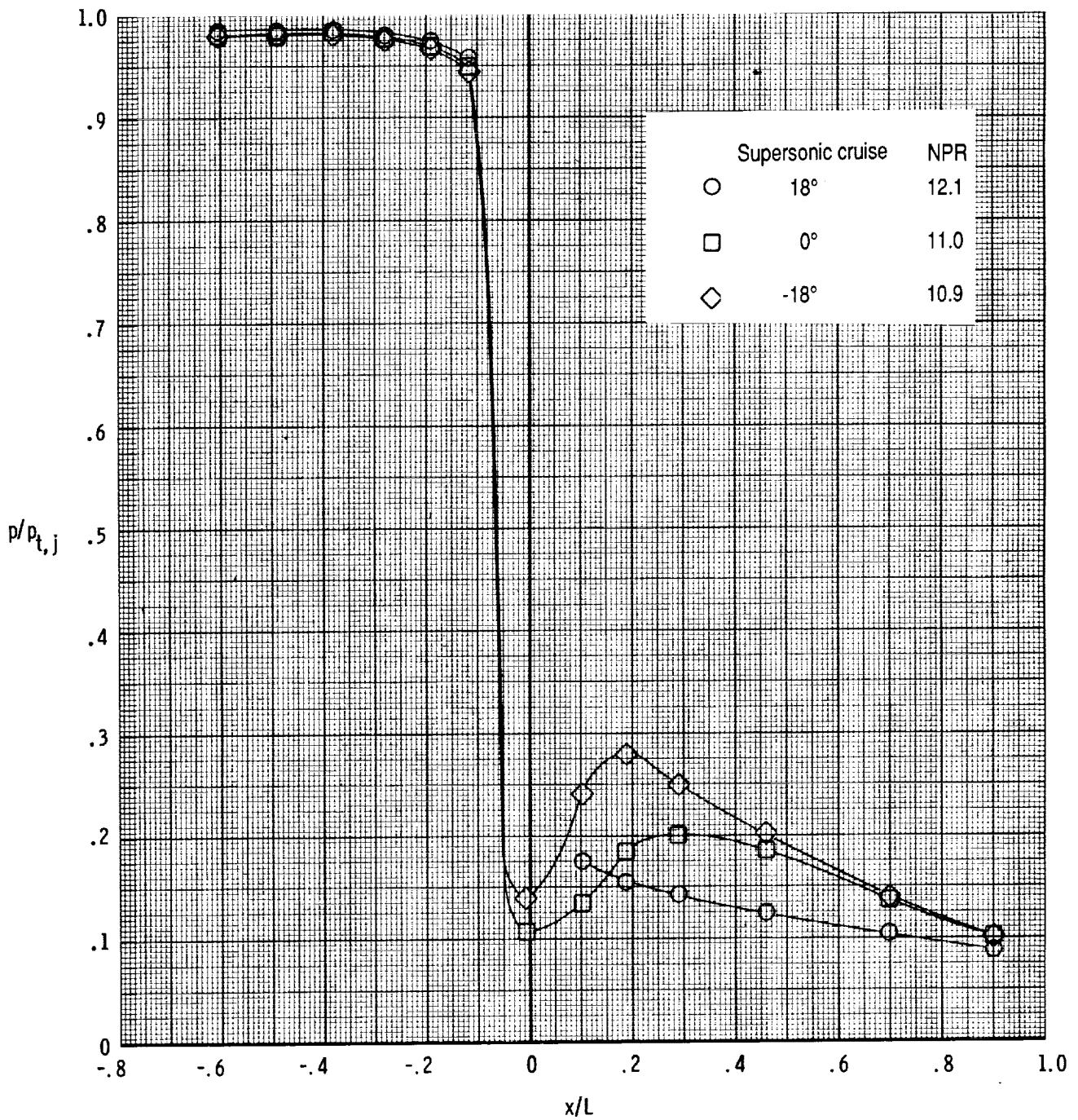
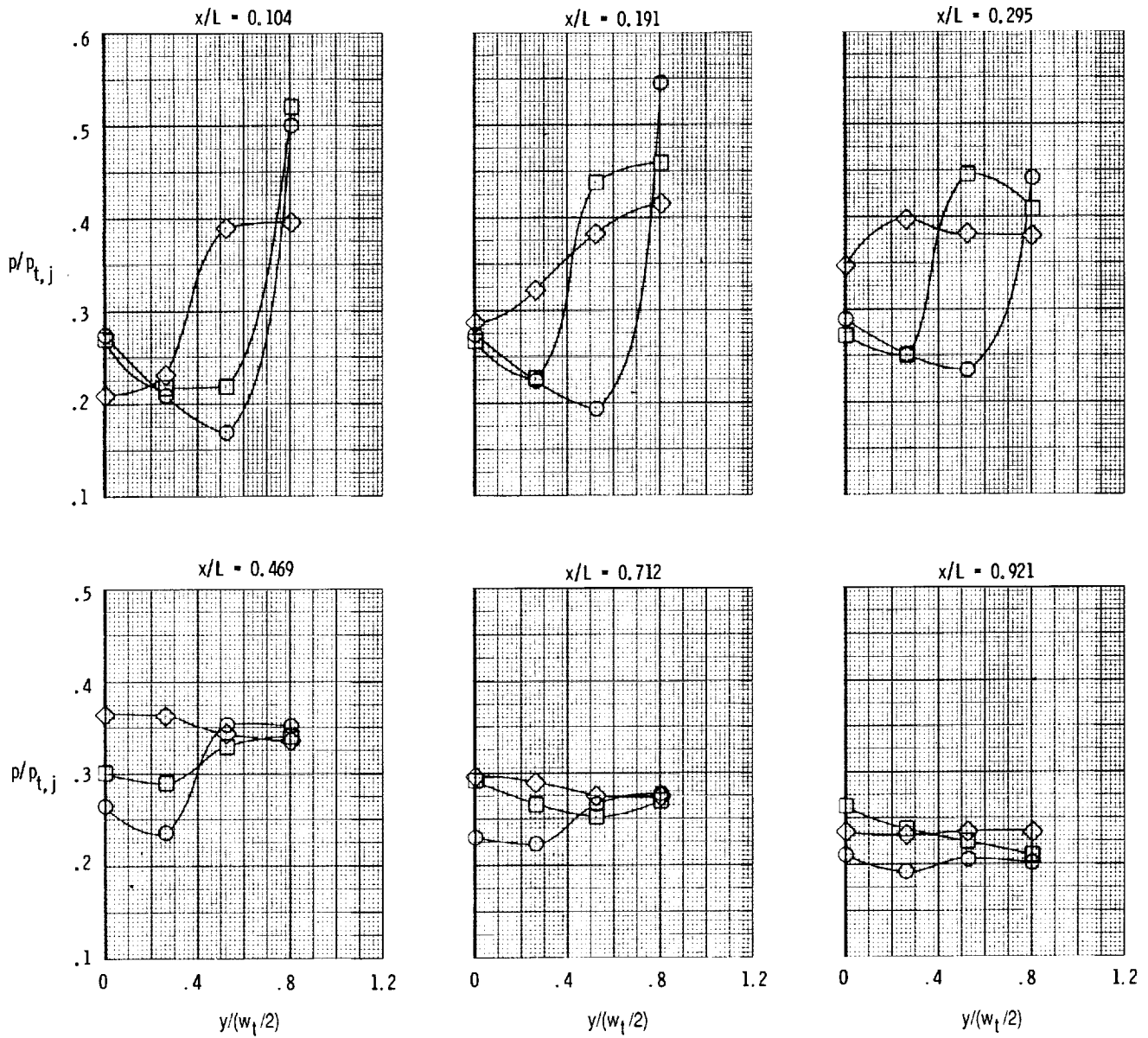(a) Convergent and divergent flap centerline distributions.

Figure 9. Static pressure distributions for dry power supersonic cruise configurations at a NPR near peak performance.
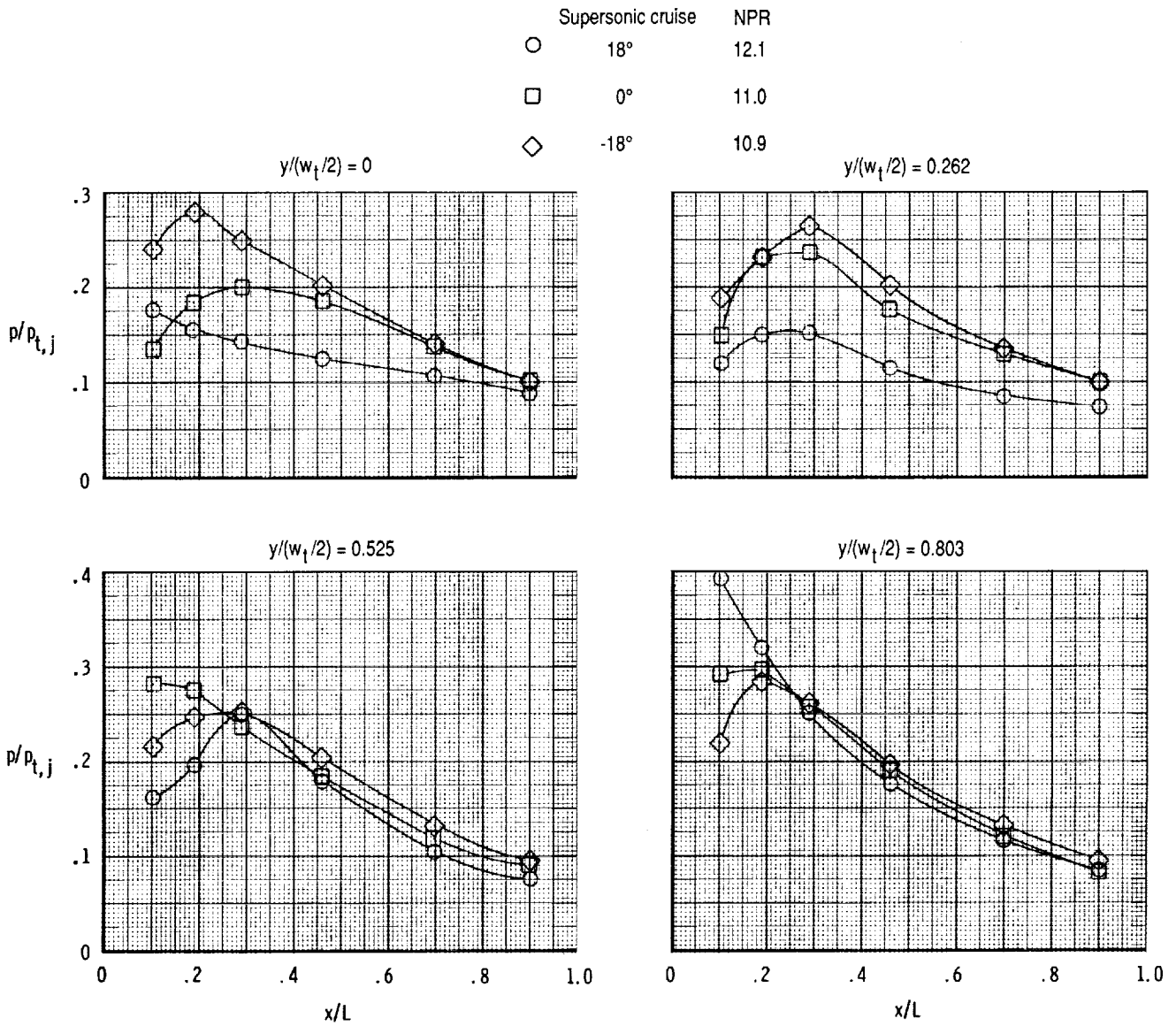
(b) Divergent flap distributions at different spanwise locations.

Figure 9. Continued.
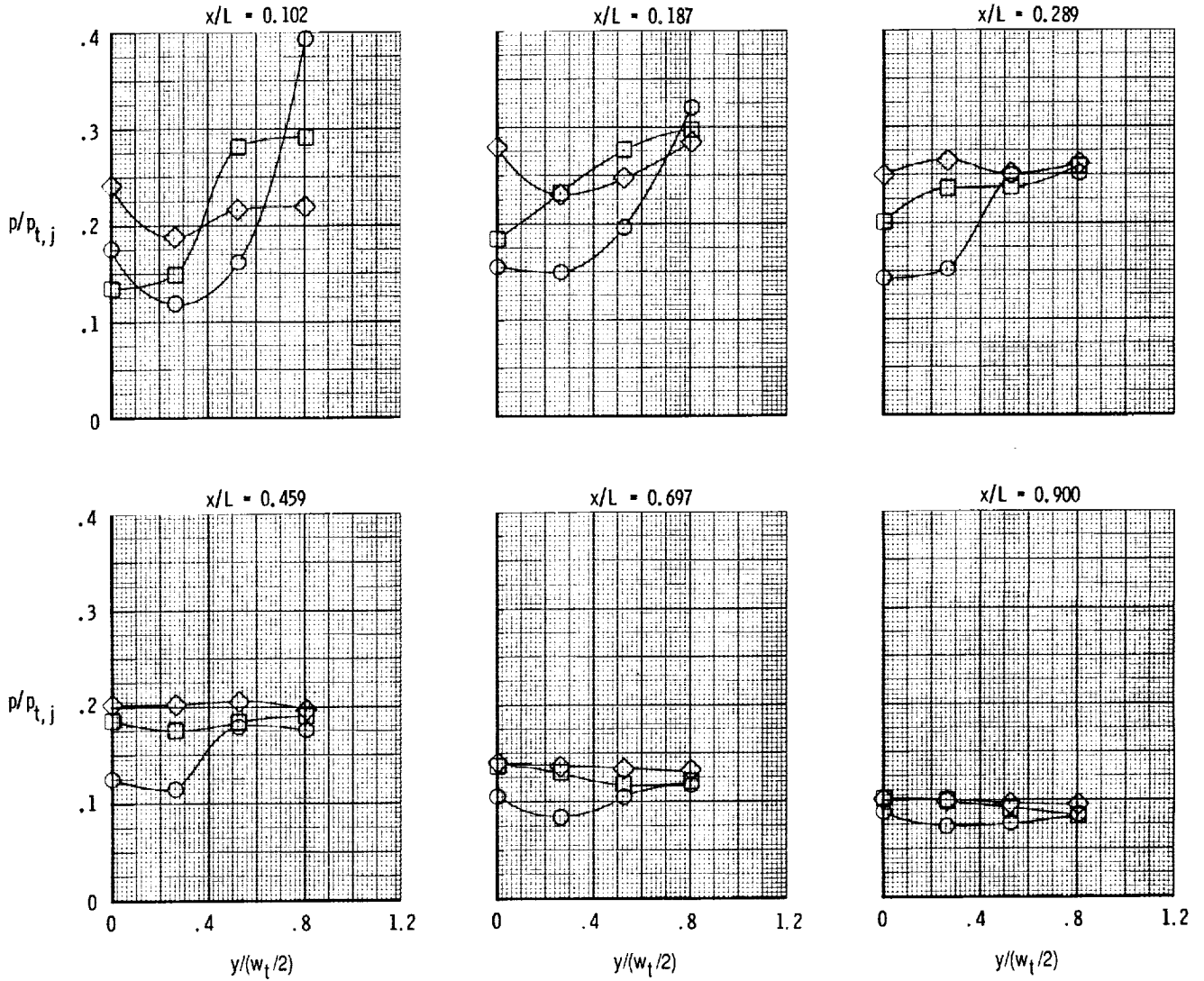
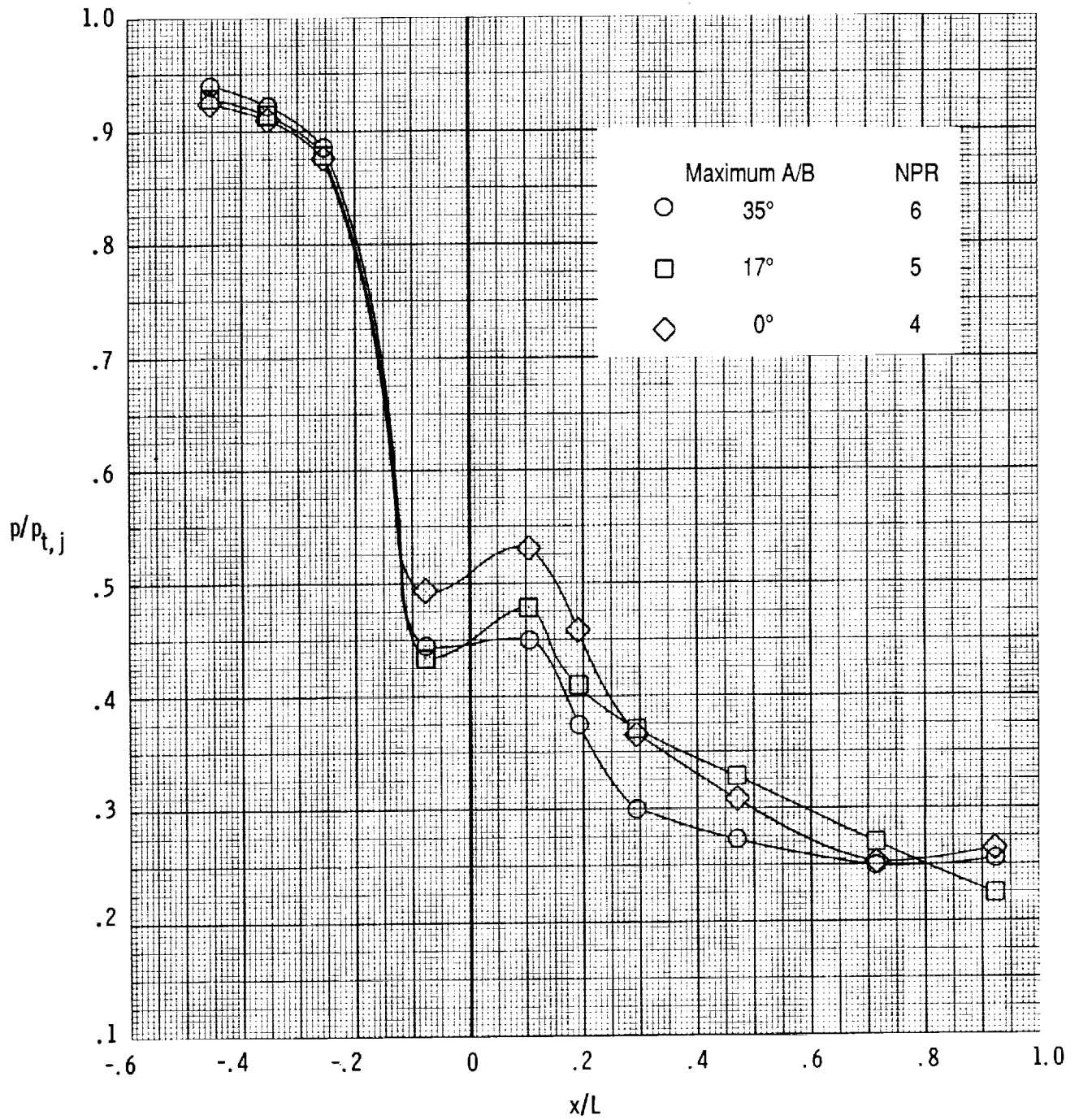(c) Divergent flap lateral distributions.

Figure 9. Continued.
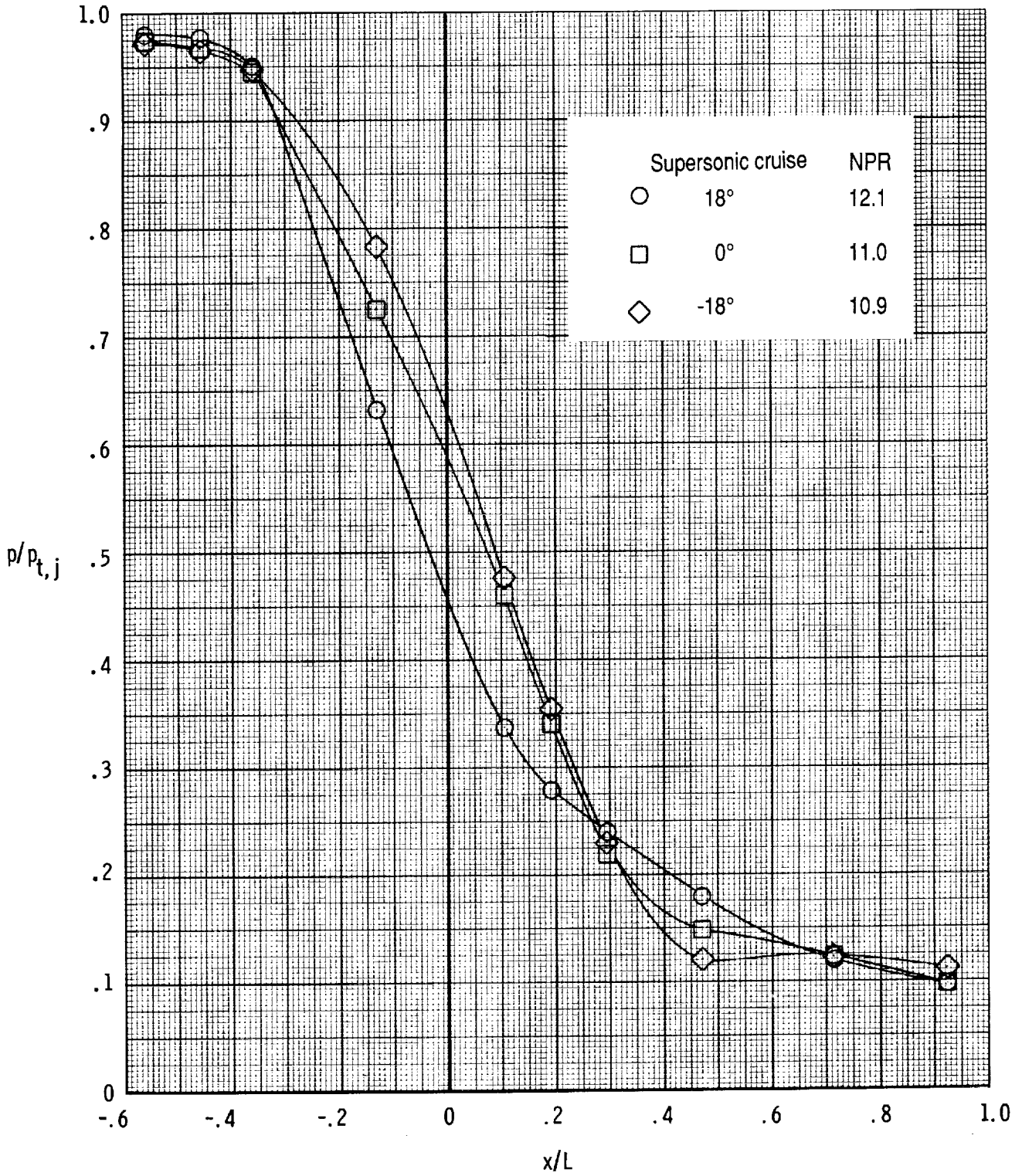
(d) Sidewall centerline distributions.

Figure 9. Concluded.
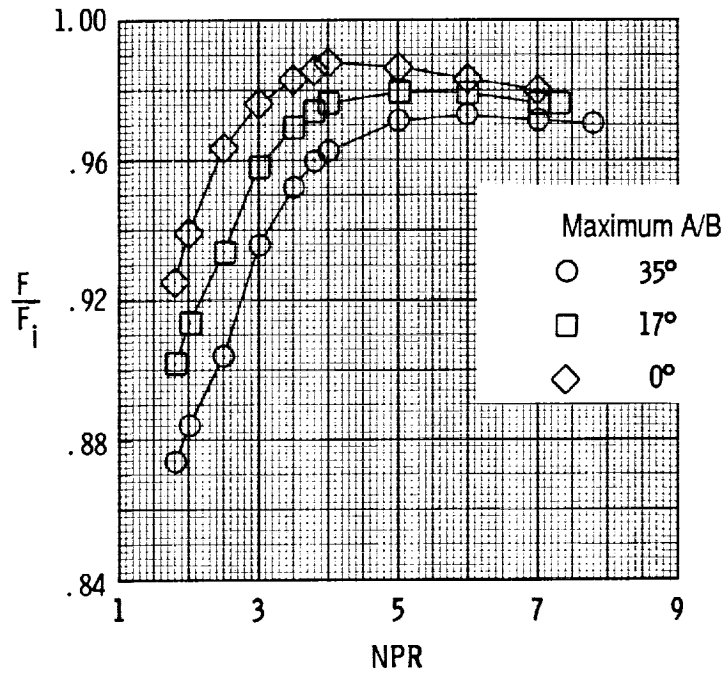
(a) Internal thrust ratio curves.

(b) Discharge coefficient curves.

Figure 10. Nozzle internal performance for maximum A/B power configurations.

(a) Convergent and divergent flap centerline distributions.

Figure 11. Static pressure distributions for maximum A/B power configurations at a NPR near peak performance.
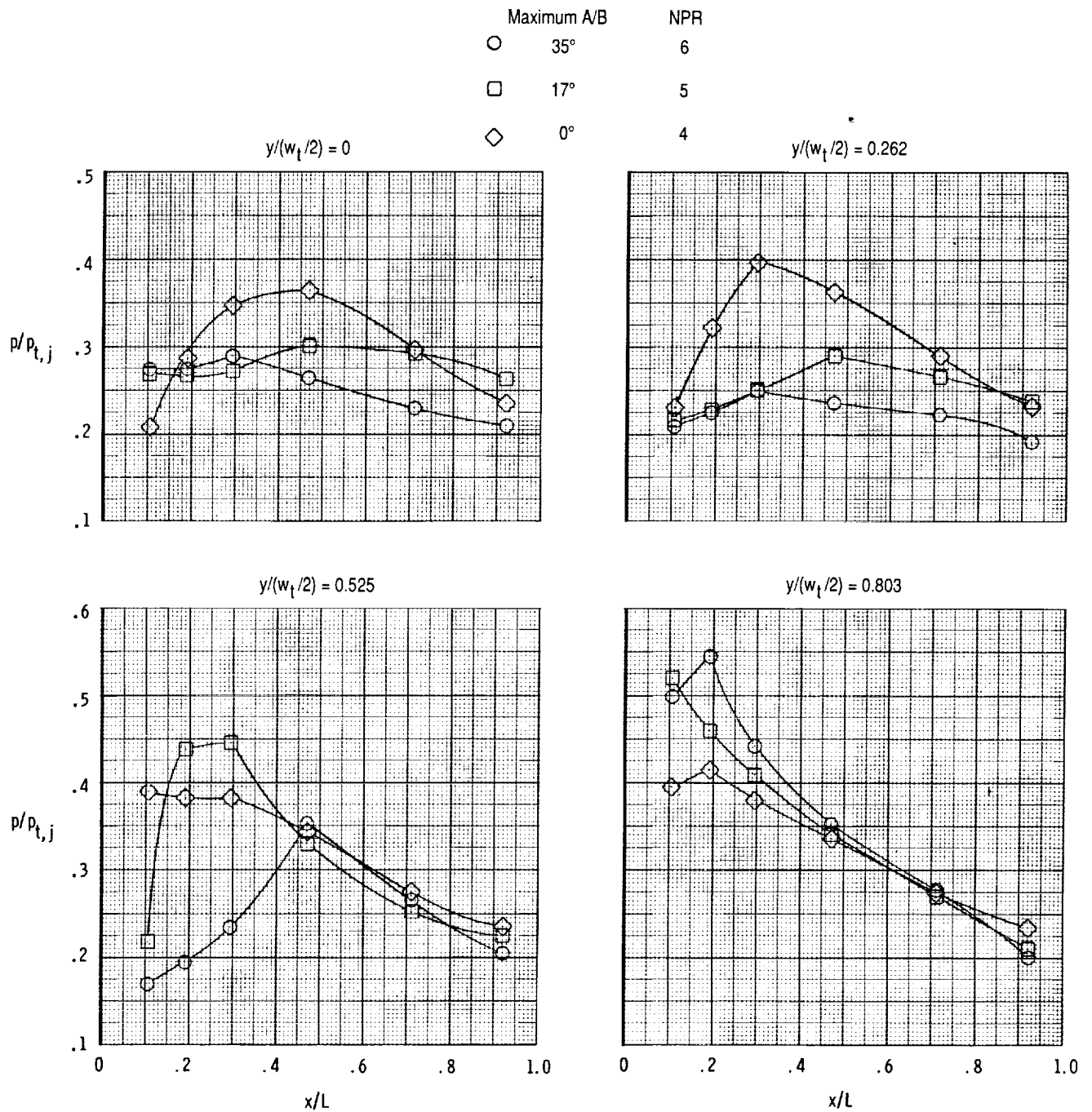
(b) Divergent flap distributions at different spanwise locations.

Figure 11. Continued.

(c) Divergent flap lateral distributions.

Figure 11. Continued.

(d) Sidewall centerline distributions.

Figure 11. Concluded.

Report Documentation Page

1. Report No. NASA TM-4230	2. Government Accession No.	3. Recipient's Catalog No.
4. Title and Subtitle Internal Performance of a Hybrid Axisymmetric/ Nonaxisymmetric Convergent-Divergent Nozzle		5. Report Date January 1991
		6. Performing Organization Code
7. Author(s) John G. Taylor		8. Performing Organization Report No. L-16816
9. Performing Organization Name and Address NASA Langley Research Center Hampton, VA 23665-5225		10. Work Unit No. 505-62-71-01
		11. Contract or Grant No.
12. Sponsoring Agency Name and Address National Aeronautics and Space Administration Washington, DC 20546-0001		13. Type of Report and Period Covered Technical Memorandum
		14. Sponsoring Agency Code

15. Supplementary Notes

16. Abstract

An investigation has been conducted in the static test facility of the Langley 16-Foot Transonic Tunnel to determine the internal performance of a hybrid axisymmetric/nonaxisymmetric nozzle in forward-thrust mode. Nozzle cross sections in the spherical convergent section were axisymmetric, whereas cross sections in the divergent flap area were nonaxisymmetric (two dimensional). Nozzle concepts simulating dry and afterburning power settings were investigated. Both subsonic cruise and supersonic cruise expansion ratios were tested for the dry power nozzle concepts. Afterburning power configurations were tested at an expansion ratio typical of subsonic acceleration. The spherical convergent flaps were designed in such a way that the transition from axisymmetric to nonaxisymmetric cross section occurred in the region of the nozzle throat. Three different nozzle throat geometries were tested for each nozzle power setting. High-pressure air was used to simulate the jet exhaust at nozzle pressure ratios up to 12.

17. Key Words (Suggested by Authors(s)) Convergent-divergent nozzle Internal performance Thrust Nozzle	18. Distribution Statement Unclassified—Unlimited Subject Category 02		
19. Security Classif. (of this report) Unclassified	20. Security Classif. (of this page) Unclassified	21. No. of Pages 55	22. Price A04